Stimulated Raman amplification in GaAs/AlAs intermixed superlattices

Isao Tomita,[1,2,*] Shinichi Saito,[1,3] and David C. Hutchings[4]

[1]*Nanoelectronics & Nanotechnology Research Group,*
School of Electronics and Computer Science,
Faculty of Physical Sciences and Engineering,
University of Southampton, SO17 1BJ, UK.
[2]*Department of Electrical & Computer Engineering,*
National Institute of Technology, Gifu College, Japan.
[3]*Nanoelectronics & Nanotechnology Research Group,*
Zepler Institute, Faculty of Physical Sciences and Engineering,
University of Southampton, SO17 1BJ, UK.
[4]*Electronic and Nanoscale Engineering Group, School of Engineering,*
University of Glasgow, Glasgow G12 8QQ, UK.

Abstract

The enhancement of stimulated Raman scattering (SRS) with a GaAs/AlAs intermixed superlattice that works as a $\chi^{(3)}$-quasi-phase-matched structure is studied by taking account of Kerr-induced effects, e.g., four-wave mixing (FWM), self-phase modulation (SPM), cross-phase modulation (XPM), and two-photon absorption (TPA). In particular, the efficiency of anti-Stokes generation is enhanced here, which inherently has an extremely small efficiency due to a phase mismatch in the interaction of the pump, Stokes, and anti-Stokes waves (while the efficiency of Stokes generation is sufficiently large because of no such phase mismatch). The superlattice enhances the anti-Stokes efficiency up to the order of 10^3 when compared with that without the superlattice, particularly at a small pump intensity. In this enhancement, it is seen that there is an efficiency boost via simultaneous FWM. In this situation, it is shown how much SPM and XPM degrade the efficiency enhancement. Furthermore, an optimal superlattice length is identified that provides the highest efficiency. The degradation of the efficiency at the optimized length due to TPA is also analyzed. Finally, to gain more anti-Stokes efficiency (or control the sizes of the Stokes and anti-Stokes efficiencies), a photonic-bandgap cavity structure is proposed.

PACS numbers: 42.65.Dr, 42.65.Hw, 42.65.Wi, 71.55.Eq

---

* I.Tomita@soton.ac.uk

I. INTRODUCTION

Studies on the enhancement of stimulated Raman scattering (SRS) have been attracting a great deal of attention in recent years, aiming for its potential scientific and technological applications, e.g., probing/sensing [1, 2], optical on-chip [3–7], and telecom [8, 9] applications. Among them, the realization of SRS in silicon (Si) [3–7] gave a great impetus to the development of Si on-chip optical devices at telecom wavelengths, which provided a potential integrated optical source with Si photonics. However, there still remains an issue that large two-photon absorption (TPA) in Si at around 1.55 μm must be avoided for practical applications and yet cannot easily be resolved because the bandgap energy (1.1 eV) of Si is much smaller than the TPA energy ($2 \times 0.8 = 1.6$ eV) of 1.55-μm optical signals.

Semiconductor optical amplifiers [10] made of compound semiconductors can avoid TPA via bandgap engineering with composition-ratio and/or strain controls, but their carriers, or electron-hole pairs, that give rise to radiative recombination for optical signal amplification distort the signal waveforms via plasma effects, thus preventing the operation speed from going beyond tens of gigahertz without additional systems.

Material type	Raman gain (cm/GW)	Raman shift (nm)	Pump wavelength (nm)	Device length (mm)	Ref. No.
SiO_2	0.0065	105.6	1433	5.6×10^6	[8]
Si	20	124.8	1427	18	[4]
GaP	27	27.6	825	5.1	[11]
H_2	4.4	117.6	532	$\sim 10^3$	[12, 13]
$Ba(NO_3)_2$	47.4	29.6	532	$\sim 10^2$	[14, 15]
$Al_{0.24}Ga_{0.76}As$	10	70.8	1550	7.2	[16]

TABLE I. Properties of Raman materials.

Fortunately, silica-glass optical fibers (SiO_2, insulator with no carriers) have a wide bandgap that can avert TPA at around 1.55 μm, but their Raman gain coefficient g

(cm/GW) is very small compared with that of semiconductors, e.g., Si, GaP, AlGaAs (see Table I), thus requiring a very long fiber on the order of kilometers.

Here, we propose a compact device design that utilizes compound-semiconductor superlattices that can avoid TPA whilst utilizing the third-order optical nonlinearity enhancement, and study the enhancement behaviors from nonlinear optical physics, where the use of instantaneous nonlinear interactions (with no TPA) provides this superlattice device with potential that goes beyond the current operation limitations of Si-photonic devices and semiconductor optical amplifiers.

A. Research target, method, and applications

In this paper, we focus on a merit of our device that can boost the output efficiency of the anti-Stokes waves that originally have a vanishingly small efficiency due to a large phase mismatch $\Delta \boldsymbol{k} = 2\boldsymbol{k}_0 - \boldsymbol{k}_{-1} - \boldsymbol{k}_1$ that arises in the interacting pump, Stokes, and anti-Stokes waves of wavevectors $\boldsymbol{k}_0$, $\boldsymbol{k}_{-1}$, and $\boldsymbol{k}_1$, respectively [17]. Fortunately, the Stokes waves are strongly generated in this device because of the absence of such phase mismatch requirement. For example, the ratio of the anti-Stokes-wave power to the Stokes-wave power, e.g., in Si waveguides, is only 10^{-5} - 10^{-6} [18, 19]. But our proposed device should provide the same order of output power for both Stokes and anti-Stokes waves, as will be seen in §IV B 4. An application of the anti-Stokes-wave amplification with our device is that, since it generates a short wavelength (e.g., 1.49 μm) from an input pump beam (e.g., at 1.56 μm), it can amplify the downstream signals at 1.49 μm in gigabit-ethernet passive optical networks (GE-PONs) [20]. It can also be used for channel conversion and amplification in wavelength-division multiplexing (WDM) systems.

To attain high amplification by removal of $\Delta \boldsymbol{k}$, we employ quasi-phase matching (QPM) [21] for $\chi^{(3)}$-processes, in a collinear beam configuration (e.g., in a waveguide) that gives a strong field coupling among those three waves and thus achieves high output efficiency. In this paper, instead of QPM structures proposed in SiO_2, $Ba(NO_3)_2$, and H_2 [12, 14], which are not easily fabricated, we employ a GaAs/AlAs intermixed superlattice, which was originally developed as a $\chi^{(2)}$-periodic QPM structure [22]. This has a small refractive-index change (~ 0.01) in $\chi^{(2)}$-domains (i.e., only a 0.3 % change compared with the average refractive index in the periodic structure) [23], and has an advantage of avoiding significant additional optical scattering loss caused by interface roughness between the discrete $\chi^{(2)}$-domains in orientation-patterned AlGaAs structures [24].

An important aspect in the GaAs/AlAs intermixed superlattice is that it also works as a $\chi^{(3)}$-periodic QPM structure because a $\chi^{(3)}$-change is also induced in a similar way to the $\chi^{(2)}$-change caused by blue-shifted resonance in nonlinear susceptibility [25]. The removal of $\Delta\boldsymbol{k}$ with this $\chi^{(3)}$-periodic structure realizes strong anti-Stokes-wave generation. Although the above $\chi^{(3)}$-periodic superlattice still has $\chi^{(2)}$-periodicity, the anti-Stokes waves are not influenced, e.g., by difference-frequency generation with $\chi^{(2)}$, when the $\chi^{(3)}$-period Λ is set such that $|2\boldsymbol{k}_0 - \boldsymbol{k}_{-1} - \boldsymbol{k}_1| = 2\pi/\Lambda$, because difference-frequency generation requires $|\boldsymbol{k}_0 - \boldsymbol{k}_{-1} - \boldsymbol{k}_1| = 2\pi/\Lambda$.

B. Device physics research

In our semiconductor $\chi^{(3)}$-periodic structure, we carefully examine the anti-Stokes-wave generation in terms of a pump intensity and a device length from our interest in highly-efficient output with a moderate pump intensity and a reasonable device length.

Furthermore, we carefully examine other nonlinear effects (Kerr-induced effects), such as four-wave mixing (FWM), self-phase modulation (SPM), cross-phase modulation (XPM), because these are much greater than those in Si. As for two-photon absorption (TPA), since the bandgap energy in the GaAs/AlAs superlattice is comparable to the TPA energy (1.6 eV), TPA can be avoided by subtle input-wavelength adjustment or bandgap engineering, which can be done easily when compared with the Si case.

The influence of stimulated Brillouin scattering (SBS) coupled with low-frequency acoustic-phonon modes is neglected here, because the Brillouin-shifted frequency and its linewidth are only $f_{\mathrm{SBS}} \sim 20$ GHz and $\Delta f_{\mathrm{SBS}} \sim 170$ MHz, e.g., in GaAs [26], respectively. Thus if we use relatively short input pulses (e.g., with a width of ~ 10 ps or a spectral width of ~ 100 GHz used often in optical communications), then SBS nearly ceases to occur, because most of the spectral components are out of the SBS gain linewidth Δf_{SBS}. This SBS-stopping phenomenon is well known in optical fibers for short pump pulses [27]. On the other hand, since SRS coupled with high-frequency optical-phonon modes has a much wider gain linewidth $\Delta f_{\mathrm{SRS}} \sim 100$ GHz, SRS can keep its large gain, e.g., for the 10-ps pulses, at the Raman-shifted frequency $f_{\mathrm{SRS}} \sim 9$ THz [16].

In this way, by including such nonlinear interactions as optical Raman and Kerr effects in the proposed periodic structure, we examine the SRS efficiency; more specifically, that of SRS for anti-Stokes waves with a far smaller efficiency than that of Stokes waves.

C. Paper structure

After this Introduction section (§I), we show a model for the periodic GaAs/AlAs intermixed superlattice in §II. We then derive coupled nonlinear equations that deal with the interacting pump, Stoke- and anti-Stokes waves in the superlattice in §III. In §IV, we obtain analytical solutions with some approximations to the coupled equations to see the properties of those nonlinear effects on the output efficiency. Furthermore, we obtain numerical solutions that contain no such approximations, and compare them with the analytical solutions to check numerical accuracy. The numerical computations give the efficiency when there is the superlattice, which is compared with the efficiency without the superlattice, and improvements are discussed. Finally, §V is devoted to summary.

II. MODEL FOR $\chi^{(3)}$-PERIODIC SUPERLATTICE

We show our device model that contains a periodic GaAs/AlAs intermixed superlattice in Fig. 1, where the pump, Stokes and anti-Stokes wavelengths are larger than the half-bandgap wavelength of the superlattice, which prevents TPA. (The influence of TPA will be examined in detail in §IV B 7.)

In case where one of those three wavelengths is shorter than the half-bandgap wavelength, strong TPA will emerge, and considerable free carrier absorption (FCA) will also emerge due to TPA-induced carriers. In this case, we use a reverse-biased p-n junction embedded in the device to avert FCA, as shown in Fig.1, where the superlattice waveguide is sandwiched between buffer layers of $\mathrm{Al}_x\mathrm{Ga}_{1-x}\mathrm{As}$ with $x = 0.56, 0.6$ [23] with a lower refractive index than that of the waveguide. If those three wavelengths are longer than the half-bandgap wavelength, such a p-n junction is not necessary (or no bias-voltage application is necessary for the p-n junction).

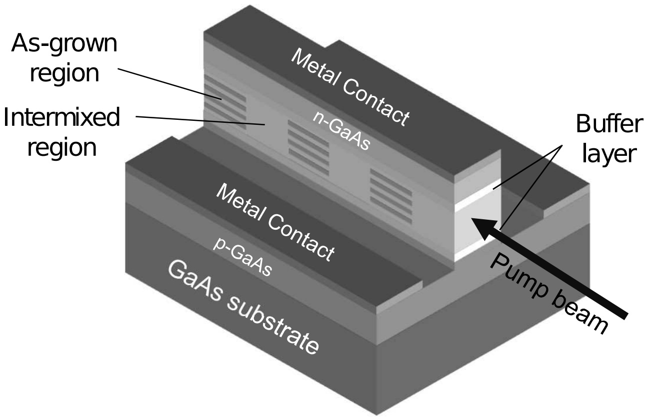

FIG. 1. Device structure. A GaAs/AlAs superlattice waveguide containing periodic as-grown and intermixed regions is sandwiched between buffer layers that have a lower refractive index than that of the waveguide to confine light in it, where the thickness of the buffer layers is adjusted to strongly confine the light, and the waveguide together with the buffer layers is also sandwiched between p-GaAs and n-GaAs to form a p-n junction.

When the as-grown domains of the waveguide in Fig. 1 are made of a 14:14 monolayer GaAs/AlAs superlattice, the $\chi^{(3)}$ characteristic can be well approximated by that of $\mathrm{Al}_x\mathrm{Ga}_{1-x}\mathrm{As}$ ($x = 0.18$) [28], which has a fundamental absorption edge almost identical to that of the 14:14 monolayer GaAs/AlAs superlattice. In our calculations for the GaAs/AlAs as-grown domains, we use this $\mathrm{Al}_x\mathrm{Ga}_{1-x}\mathrm{As}$ ($x = 0.18$), which makes the calculations simpler.

On the other hand, the intermixed regions have a blue-shifted absorption edge as regards the $\chi^{(3)}$-property, and the $\chi^{(3)}$ value is considerably decreased when compared with that in the as-grown domains (actually it is nearly a half of $\chi^{(3)}$) [28]. We set this value to be $\varepsilon\chi^{(3)}$ ($0 \le \varepsilon \le 1$) in our calculations, as will be shown in §IV B 4. In the next section, we derive coupled nonlinear equations to describe the evolution of the pump, Stokes and anti-Stokes waves for the above waveguide device.

III. COUPLED NONLINEAR EQUATIONS FOR THE DEVICE

In deriving the coupled nonlinear equations, we assume that stimulated Raman scattering (SRS) is greater in photon generation than spontaneous Raman scattering (i.e., beyond the SRS threshold power) [17]. In this case, since there is almost no difference in optical power obtained by classical and quantum analyses, we describe SRS in the waveguide device with classical wave equations derived from Maxwell's equations that are coupled with molecular vibrations in the employed semiconductor.

To perform the analysis for SRS, we start with the following wave equation obtained via the standard procedure [29].

$$\nabla^2 E - \frac{1}{c^2}\frac{\partial^2 E}{\partial t^2} = \mu_0 \frac{\partial^2}{\partial t^2}\left(P_{\mathrm{LN}} + P_{\mathrm{NL}}\right), \tag{1}$$

$$\nabla^2 E - \frac{1}{c^2}\frac{\partial^2 (\epsilon E)}{\partial t^2} = \mu_0 \frac{\partial^2 P_{\mathrm{NL}}}{\partial t^2}. \tag{2}$$

Here, $\nabla^2 = \partial^2/\partial x^2 + \partial^2/\partial y^2 + \partial^2/\partial z^2$. The waveguide is set parallel to the z direction. $E = E(z,t)$ is the electric field of the coupled three waves (i.e., the pump, Stokes, and anti-Stokes waves) that propagate in the z direction. P_{LN} is the linear polarization defined by $P_{\mathrm{LN}} = \epsilon_0\chi^{(0)}E$ with the vacuum permittivity ϵ_0 and the linear susceptibility $\chi^{(0)}$. The relative permittivity ϵ is related to $\chi^{(0)}$ as $\epsilon = \epsilon_0(1+\chi^{(0)})$ that gives the refractive index n as $n = \sqrt{\epsilon/\epsilon_0}$. P_{NL} is the nonlinear polarization containing the Raman and Kerr effects. μ_0 is the magnetic permeability. For non-magnetic semiconductors (e.g., $\mathrm{Al}_x\mathrm{Ga}_{1-x}\mathrm{As}$), they have the same value μ_0 in vacuum. c is the velocity of light that has the relation with ϵ_0 and μ_0 as $c = 1/\sqrt{\epsilon_0\mu_0}$. In the above, TE polarization has been assumed for E, P_{LN}, and P_{NL}, which are excited by TE-mode pump lasers.

The nonlinear polarization for the Raman effect is given by [14, 30]

$$P_{\mathrm{NL}}^{\mathrm{R}} = \epsilon_0 \chi'^{(3)} Q E, \tag{3}$$

$$\frac{\partial^2 Q}{\partial t^2} + \frac{2}{\tau}\frac{\partial Q}{\partial t} + \omega_\nu^2 Q = \gamma E^2. \tag{4}$$

Here, $\chi'^{(3)}$ is the imaginary part of the third-order nonlinear susceptibility. Q is the phonon-wave amplitude. ω_ν is the Raman frequency. τ is the relaxation time of the molecular oscillation. γ is a constant that characterizes the coupling between electric fields and polarized molecules. In addition, the nonlinear polarization for the Kerr effect is given by [27]

$$P_{\mathrm{NL}}^{\mathrm{K}} = \epsilon_0 \chi^{(3)} E^3, \tag{5}$$

where $\chi^{(3)}$ is the real part of the third-order nonlinear susceptibility. Experimentally, the Kerr effect arises together with the Raman effect [31], and thus the total nonlinear polarization P_{NL} is expressed as the sum of Eqs. (3) and (5).

In the above, a choice of the tensor component in the third-order nonlinear susceptibility is taken so that TE-mode input gives TE-mode output.

A. Simplification of the space and time derivatives of the wave equation

The space and time derivatives in the left-hand side of the wave equation Eq. (2) are simplified when we use an optical pulse with its spatial width larger than a characteristic length of the waves (i.e., the wavelength). This is known as the slowly-varying-envelope approximation [29]. We use this approximation throughout the paper.

To express ϵE in Eq. (2) containing the three waves, we use the following sum of electric fields.

$$\epsilon E = \frac{1}{2}\left(\sum_j \epsilon_j E_j \, e^{i(k_j z - \omega_j t)} + \text{c.c.}\right), \tag{6}$$

where $j = -1, 0, 1$ stand for the Stokes, pump, and anti-Stokes waves, respectively, ω_j is the frequency of the j-th wave, and ϵ_j is the ω_j-component of ϵ, i.e., $\epsilon_j = \epsilon(\omega_j)$. k_j is the wavenumber of the j-th wave. Using the Raman frequency ω_ν, we can write ω_j as

$\omega_j = \omega_0 + j\omega_\nu$. The Stokes and anti-Stokes waves ($j = -1, 1$) that we deal with here are the first excited ones. Since the growth of higher excited waves than the first excited waves needs a much longer interaction length than that for the first exited waves [14], and since we are interested in a relatively short waveguide on the order of a centimeter, the emergence of higher excited waves is ignored.

In addition to Eq. (6), if we set $\epsilon = \epsilon_j = 1$ in it, the expansion of E takes the form.

$$E = \frac{1}{2}\left(\sum_j E_j\, e^{i(k_j z - \omega_j t)} + \text{c.c.}\right). \tag{7}$$

In Eq. (2), we insert Eq. (6) into $\partial^2(\epsilon E)/\partial t^2$ and Eq. (7) into $\nabla^2 E$, where a relation $\partial^2 E/\partial x^2 = \partial^2 E/\partial y^2 = 0$ holds because of the assumption $E = E(z, t)$. The spread of the electric fields in the x and y directions is included as a constant cross-sectional area of the waveguide.

A simplified equation in the left-hand side of Eq. (2) by substituting Eq. (7) for $\partial^2 E/\partial z^2$ is of the form.

$$\begin{aligned}\frac{\partial^2 E}{\partial z^2} &= \frac{1}{2}\left(\sum_j \frac{\partial^2 E_j}{\partial z^2} e^{i(k_j z - \omega_j t)} + 2\sum_j ik_j \frac{\partial E_j}{\partial z} e^{i(k_j z - \omega_j t)} - \sum_j k_j^2 E_j\, e^{i(k_j z - \omega_j t)} + \text{c.c.}\right)\\ &\approx \sum_j ik_j \frac{\partial E_j}{\partial z} e^{i(k_j z - \omega_j t)} - \sum_j \frac{k_j^2}{2} E_j\, e^{i(k_j z - \omega_j t)} + \text{c.c.}.\end{aligned} \tag{8}$$

Also, by substituting Eq. (6) for $\partial^2(\epsilon E)/\partial t^2$, we obtain

$$\frac{\partial^2(\epsilon E)}{\partial t^2} \approx -\sum_j i\epsilon_j \omega_j \frac{\partial E_j}{\partial t} e^{i(k_j z - \omega_j t)} - \sum_j \epsilon_j \frac{\omega_j^2}{2} E_j e^{i(k_j z - \omega_j t)} + \text{c.c.}. \tag{9}$$

Inserting Eqs. (8) and (9) into the left-hand side of Eq. (2) with the relation $\epsilon_j = n_j^2$ (n_j is the refractive index for the j-th wave), we obtain

$$\begin{aligned}\nabla^2 E - \frac{1}{c^2}\frac{\partial^2(\epsilon E)}{\partial t^2} &\approx \sum_j e^{i(k_j z - \omega_j t)} \left(ik_j \frac{\partial}{\partial z} + i\frac{n_j^2}{c^2}\omega_j \frac{\partial}{\partial t}\right) E_j + \text{c.c.}\\ &= \sum_j e^{i(k_j z - \omega_j t)} ik_j \left(\frac{\partial}{\partial z} + \frac{n_j}{c}\frac{\partial}{\partial t}\right) E_j + \text{c.c.},\end{aligned} \tag{10}$$

where the relation $\omega_j = (c/n_j)k_j$ was used. By replacing n_j ($j = -1, 0, 1$) with the averaged value $n = \langle n_j \rangle$ in Eq. (10), we can further simplify the space and time derivatives of Eq. (10). This replacement does not severely affect the results because a refractive-index deviation

($\Delta n \approx 0.01$) from n is only 0.3 % of $n = \langle n_j \rangle = 3.09$, which is obtained from $n_j \approx 3.08$ - 3.10 at 1450 - 1600 nm [23]. We then use the transformations, $z_{\text{new}} = z_{\text{old}}$, $t_{\text{new}} = t_{\text{old}} - (n/c)z_{\text{old}}$ [27], and obtain

$$ik_j \left(\frac{\partial}{\partial z} + \frac{n}{c}\frac{\partial}{\partial t} \right) E_j = ik_j \frac{\partial}{\partial z} E_j. \tag{11}$$

This transformation corresponds to a frame change that the optical pulse in the waveguide is observed from a moving coordinate in the z direction with a velocity of c/n.

B. Derivation of terms for the Raman effect

To derive the coupled equations of the three waves with $j = -1, 0, 1$, we first need to extract nonlinear polarization terms for the Raman effect that satisfy $\omega_0 - \omega_{-1} = \omega_\nu$ and $\omega_1 - \omega_0 = \omega_\nu$, which we call resonant terms. Here, ω_{-1}, ω_0, and ω_1 stand for the frequencies of the Stokes, pump, and anti-Stokes waves, respectively. The relation of ω_{-1}, ω_0, ω_1, and ω_ν is illustrated in Fig. 2.

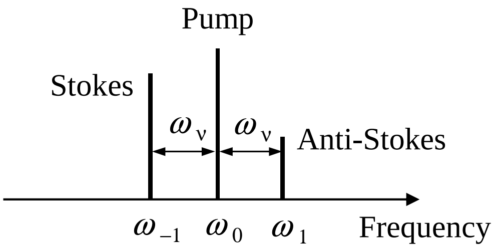

FIG. 2. Relation of ω_{-1}, ω_0, ω_1, and ω_ν.

To calculate the nonlinear polarization in Eq. (3), we insert the electric field E of Eq. (7) and the following phonon-wave amplitude Q

$$Q = \frac{1}{2}\left(q\, e^{i(k_\nu z - \omega_\nu t)} + \text{c.c.} \right), \tag{12}$$

into Eq. (3), where k_ν is the wavenumber of the phonon wave with a frequency of ω_ν. By this insertion, we have

$$P_{\text{NL}}^{\text{R}} = \frac{\epsilon_0 \chi'^{(3)}}{4} \left(\sum_j qE_{j-1}\, e^{i((k_{j-1}+k_\nu)z - \omega_j t)} + q^* E_{j+1}\, e^{i((k_{j+1}-k_\nu)z - \omega_j t)} + \text{c.c.} \right). \tag{13}$$

Next, we perform the second-order time derivative of $P_{\mathrm{NL}}^{\mathrm{R}}$ that is necessary for the calculation of the right-hand side of Eq. (2), and we have

$$\mu_0 \frac{\partial^2 P_{\mathrm{NL}}^{\mathrm{R}}}{\partial t^2} \approx -\frac{\epsilon_0 \mu_0 \chi'^{(3)}}{4} \Bigg(\sum_j \omega_j^2 q E_{j-1}\, e^{i((k_{j-1}+k_\nu)z-\omega_j t)} + \omega_j^2 q^* E_{j+1}\, e^{i((k_{j+1}-k_\nu)z-\omega_j t)} + \mathrm{c.c.} \Bigg), \tag{14}$$

where the slowly-varying-envelope approximations, $|\omega_j q| \gg |\partial q/\partial t|$, $|\omega_j E_j| \gg |\partial E_j/\partial t|$, were used.

To extract resonant terms from Eq. (14) for ω_j ($j = -1, 0, 1$), we write down the terms resonant to ω_j in Eq. (13) as $P_{\mathrm{R}}^{(\omega_j)}$ and obtain $\mu_0 \partial^2 P_{\mathrm{R}}^{(\omega_j)}/\partial t^2$ for $j = -1, 0, 1$ as

$$\mu_0 \frac{\partial^2 P_{\mathrm{R}}^{(\omega_{-1})}}{\partial t^2} = -\frac{\epsilon_0 \mu_0 \chi'^{(3)}}{4} \omega_{-1}^2\, q^* E_0\, e^{i((k_0-k_\nu)z-\omega_{-1} t)}, \tag{15}$$

$$\mu_0 \frac{\partial^2 P_{\mathrm{R}}^{(\omega_0)}}{\partial t^2} = -\frac{\epsilon_0 \mu_0 \chi'^{(3)}}{4} \omega_0^2 \left(q E_{-1}\, e^{i((k_{-1}+k_\nu)z-\omega_0 t)} + q^* E_1\, e^{i((k_1-k_\nu)z-\omega_0 t)} \right), \tag{16}$$

$$\mu_0 \frac{\partial^2 P_{\mathrm{R}}^{(\omega_1)}}{\partial t^2} = -\frac{\epsilon_0 \mu_0 \chi'^{(3)}}{4} \omega_1^2\, q E_0\, e^{i((k_0+k_\nu)z-\omega_1 t)}. \tag{17}$$

The q and q^* in Eqs. (15), (16), and (17) are related to E_j via Eqs. (4) and (12). To clarify the relation between them, we calculate Eq. (4) by inserting Eq. (12) into it. This calculation needs the first- and the second-order time derivatives of Q, which are of the form.

$$\frac{\partial Q}{\partial t} = \frac{1}{2} \left(\frac{\partial q}{\partial t} e^{i(k_\nu z-\omega_\nu t)} - i\omega_\nu q\, e^{i(k_\nu z-\omega_\nu t)} + \mathrm{c.c.} \right), \tag{18}$$

$$\begin{aligned} \frac{\partial^2 Q}{\partial t^2} &= \frac{1}{2} \left(\frac{\partial^2 q}{\partial t^2} e^{i(k_\nu z-\omega_\nu t)} - 2i\omega_\nu \frac{\partial q}{\partial t} e^{i(k_\nu z-\omega_\nu t)} - \omega_\nu^2 q\, e^{i(k_\nu z-\omega_\nu t)} + \mathrm{c.c.} \right) \\ &\approx \frac{1}{2} \left(-2i\omega_\nu \frac{\partial q}{\partial t} e^{i(k_\nu z-\omega_\nu t)} - \omega_\nu^2 q\, e^{i(k_\nu z-\omega_\nu t)} + \mathrm{c.c.} \right) \\ &= -\left(i\omega_\nu \frac{\partial q}{\partial t} + \frac{\omega_\nu^2}{2} q \right) e^{i(k_\nu z-\omega_\nu t)} + \mathrm{c.c.}, \end{aligned} \tag{19}$$

where the slowly-varying-envelope approximation was used again.

To obtain the relation between q (or q^*) and E_j, we substitute Eqs. (18) and (19) for Eq. (4) and obtain

$$\left[\left(-i\omega_\nu + \frac{1}{\tau} \right) \frac{\partial q}{\partial t} - i\frac{\omega_\nu}{\tau} q \right] e^{i(k_\nu z-\omega_\nu t)} + \mathrm{c.c.} = \gamma E^2, \tag{20}$$

$$-i\omega_\nu \left(\frac{\partial q}{\partial t} + \frac{q}{\tau} \right) e^{i(k_\nu z-\omega_\nu t)} + \mathrm{c.c.} = \gamma E^2, \tag{21}$$

where the approximation $\omega_\nu \gg 1/\tau$ was used, which arises from the relaxation time τ that is much greater than the time scale ($\sim 1/\omega_\nu$) of high molecular eigenfrequencies.

Next, we calculate the right-hand side of Eq. (21). Inserting Eq. (7) into it, we obtain

$$\begin{aligned}\gamma E^2 &= \gamma\left[\frac{1}{2}\left(\sum_j E_j\, e^{i(k_j z-\omega_j t)} + \text{c.c.}\right)\right]^2 \\ &= \frac{\gamma}{4}\left(\sum_j\sum_m E_j E_m\, e^{i((k_j+k_m)z-(\omega_j+\omega_m)t)}\right. \\ &\quad \left.+\sum_j\sum_m E_j E_m^*\, e^{i((k_j-k_m)z-(\omega_j-\omega_m)t)} + \text{c.c.}\right). \qquad (22)\end{aligned}$$

Extracting resonant terms from Eq. (22) that satisfy $\omega_j - \omega_m = \omega_\nu$ (or $\omega_j - \omega_{j-1} = \omega_\nu$), and substituting them for the right-hand side of Eq. (21), we obtain

$$-i\omega_\nu\left(\frac{\partial q}{\partial t} + \frac{q}{\tau}\right)e^{i(k_\nu z-\omega_\nu t)} = \frac{\gamma}{4}\sum_j E_j E_{j-1}^* e^{i((k_j-k_{j-1})z-(\omega_j-\omega_{j-1})t)}, \qquad (23)$$

$$\frac{\partial q}{\partial t} = \frac{1}{\tau}\left(-q - \frac{\gamma\tau}{4i\omega_\nu}\sum_j E_j E_{j-1}^* e^{i(k_j-k_{j-1}-k_\nu)z}\right), \qquad (24)$$

where $\omega_j - \omega_{j-1} = \omega_\nu$ was used.

For $j = -1, 0, 1$, Eq. (24) takes the form.

$$\frac{\partial q}{\partial t} = \frac{1}{\tau}\left[-q - \frac{\gamma\tau}{4i\omega_\nu}\left(E_0 E_{-1}^*\, e^{i(k_0-k_{-1}-k_\nu)z} + E_1 E_0^*\, e^{i(k_1-k_0-k_\nu)z}\right)\right]. \qquad (25)$$

Equation (25) gives the relation that connects q (or q^*) to E_j ($j = -1, 0, 1$).

C. Derivation of terms for the Kerr effect

In this section, we calculate the nonlinear polarization Eq. (5) for the Kerr effect. To do this, we substitute Eq. (7) for Eq. (5) and obtain

$$\begin{aligned}P_{\text{NL}}^{\text{K}} &= \epsilon_0\chi^{(3)}\left[\frac{1}{2}\left(\sum_j E_j\, e^{i(k_j z-\omega_j t)} + \text{c.c.}\right)\right]^3 \\ &= \frac{\epsilon_0\chi^{(3)}}{8}\left(\sum_j\sum_l\sum_m E_j E_l E_m\, e^{i((k_j+k_l+k_m)z-(\omega_j+\omega_l+\omega_m)t)}\right. \\ &\quad \left.+3\sum_j\sum_l\sum_m E_j E_l E_m^*\, e^{i((k_j+k_l-k_m)z-(\omega_j+\omega_l-\omega_m)t)} + \text{c.c.}\right). \qquad (26)\end{aligned}$$

By performing the second-order time derivative of $P_{\mathrm{NL}}^{\mathrm{K}}$ necessary to calculate the right-hand side of Eq. (2), we get

$$\mu_0 \frac{\partial^2 P_{\mathrm{NL}}^{\mathrm{K}}}{\partial t^2} \approx -\frac{\epsilon_0 \mu_0 \chi^{(3)}}{8} \left(\sum_j \sum_l \sum_m (\omega_j + \omega_l + \omega_m)^2 E_j E_l E_m \, e^{i((k_j+k_l+k_m)z - (\omega_j+\omega_l+\omega_m)t)} \right. \\ \left. +3 \sum_j \sum_l \sum_m (\omega_j + \omega_l - \omega_m)^2 E_j E_l E_m^* \, e^{i((k_j+k_l-k_m)z-(\omega_j+\omega_l-\omega_m)t)} + \text{c.c.} \right), \tag{27}$$

where the slowly-varying-envelope approximation, $|\omega_j E_j| \gg |\partial E_j / \partial t|$, was used.

To extract resonant terms from Eq. (27), we here write down the terms resonant to ω_j in Eq. (26) as $P_{\mathrm{K}}^{(\omega_j)}$ and obtain $\mu_0 \partial^2 P_{\mathrm{K}}^{(\omega_j)} / \partial t^2$ for $j = -1, 0, 1$ as

$$\mu_0 \frac{\partial^2 P_{\mathrm{K}}^{(\omega_{-1})}}{\partial t^2} = -\frac{3\epsilon_0 \chi^{(3)}}{8} \omega_{-1}^2 \left(E_{-1}|E_{-1}|^2 + 2E_{-1}|E_1|^2 + 2E_{-1}|E_0|^2 \right) e^{i(k_{-1}z - \omega_{-1}t)}, \tag{28}$$

$$\mu_0 \frac{\partial^2 P_{\mathrm{K}}^{(\omega_0)}}{\partial t^2} = -\frac{3\epsilon_0 \chi^{(3)}}{8} \omega_0^2 \left(E_0|E_0|^2 + 2E_0|E_1|^2 + 2E_0|E_{-1}|^2 \right) e^{i(k_0 z - \omega_0 t)}, \tag{29}$$

$$\mu_0 \frac{\partial^2 P_{\mathrm{K}}^{(\omega_1)}}{\partial t^2} = -\frac{3\epsilon_0 \chi^{(3)}}{8} \omega_1^2 \left(E_1|E_1|^2 + 2E_1|E_0|^2 + 2E_1|E_{-1}|^2 \right) e^{i(k_1 z - \omega_1 t)}. \tag{30}$$

In addition, because of the relation

$$\omega_0 - \omega_{-1} = \omega_1 - \omega_0 = \omega_\nu, \tag{31}$$

$$\omega_1 + \omega_{-1} - 2\omega_0 = 0, \tag{32}$$

$P_{\mathrm{K}}^{(2\omega_0 - \omega_1)}$, $P_{\mathrm{K}}^{(\omega_1 + \omega_{-1} - \omega_0)}$, and $P_{\mathrm{K}}^{(2\omega_0 - \omega_{-1})}$ are resonant to ω_{-1}, ω_0, and ω_1, respectively, and their second-order time derivatives are of the form with the addition of μ_0.

$$\begin{aligned} \mu_0 \frac{\partial^2 P_{\mathrm{K}}^{(2\omega_0-\omega_1)}}{\partial t^2} &= -\frac{3\epsilon_0 \chi^{(3)}}{8} (2\omega_0 - \omega_1)^2 \, E_0^2 E_1^* \, e^{i((2k_0 - k_1)z - (2\omega_0 - \omega_1)t)} \\ &= -\frac{3\epsilon_0 \chi^{(3)}}{8} \omega_{-1}^2 \, E_0^2 E_1^* \, e^{i((2k_0-k_1)z - \omega_{-1}t)}, \end{aligned} \tag{33}$$

$$\begin{aligned} \mu_0 \frac{\partial^2 P_{\mathrm{K}}^{(\omega_1+\omega_{-1}-\omega_0)}}{\partial t^2} &= -\frac{6\epsilon_0 \chi^{(3)}}{8} (\omega_1 + \omega_{-1} - \omega_0)^2 \, E_1 E_{-1} E_0^* \, e^{i((k_1+k_{-1}-k_0)z - (\omega_1+\omega_{-1}-\omega_0)t)} \\ &= -\frac{6\epsilon_0 \chi^{(3)}}{8} \omega_0^2 \, E_1 E_{-1} E_0^* \, e^{i((k_1+k_{-1}-k_0)z - \omega_0 t)}, \end{aligned} \tag{34}$$

$$\begin{aligned} \mu_0 \frac{\partial^2 P_{\mathrm{K}}^{(2\omega_0-\omega_{-1})}}{\partial t^2} &= -\frac{3\epsilon_0 \chi^{(3)}}{8} (2\omega_0 - \omega_{-1})^2 \, E_0^2 E_{-1}^* \, e^{i((2k_0-k_{-1})z - (2\omega_0-\omega_{-1})t)} \\ &= -\frac{3\epsilon_0 \chi^{(3)}}{8} \omega_1^2 \, E_0^2 E_{-1}^* \, e^{i((2k_0-k_{-1})z - \omega_1 t)}, \end{aligned} \tag{35}$$

where the relation Eq. (32) was used.

D. Full coupled equations with the Raman and Kerr terms

To complete building full coupled equations containing the Raman and Kerr effects, we insert the Raman terms Eqs. (15)-(17) and the Kerr terms Eqs. (28)-(30),(33)-(35) into the right-hand side of Eq. (2) and also insert Eqs. (10) and (11) into the left-hand side of Eq. (2). Using resonant terms for each ω_j ($j = -1, 0, 1$), we obtain the following coupled equations.

$$\begin{aligned}
\frac{\partial E_{-1}}{\partial z} &= i\frac{g}{2}q^* E_0 e^{i\Delta k_0 z} + i\kappa_{-1}\left(2|E_0|^2 + |E_{-1}|^2 + 2|E_1|^2\right)E_{-1} + i\kappa_{-1}E_1^* E_0^2 e^{i\Delta k z}, && (36)\\
\frac{\partial E_0}{\partial z} &= i\frac{g}{2}\frac{\omega_0}{\omega_{-1}}\left(qE_{-1}e^{-i\Delta k_0 z} + q^* E_1 e^{i\Delta k_1 z}\right)\\
&\quad + i\kappa_0\left(|E_0|^2 + 2|E_{-1}|^2 + 2|E_1|^2\right)E_0 + 2i\kappa_0 E_0^* E_{-1}E_1 e^{-i\Delta k z}, && (37)\\
\frac{\partial E_1}{\partial z} &= i\frac{g}{2}\frac{\omega_1}{\omega_{-1}}qE_0 e^{-i\Delta k_1 z} + i\kappa_1\left(2|E_0|^2 + 2|E_{-1}|^2 + |E_1|^2\right)E_1 + i\kappa_1 E_{-1}^* E_0^2 e^{i\Delta k z}, && (38)\\
\frac{\partial q}{\partial t} &= \frac{1}{\tau}\left[-q + i\left(E_0 E_{-1}^* e^{i\Delta k_0 z} + E_1 E_0^* e^{i\Delta k_1 z}\right)\right], && (39)
\end{aligned}$$

where Eq. (39) works to determine the motion of q in Eqs. (36)-(38), which is given from Eq. (25). Equations (36)-(39) have been rewritten by using the following quantities.

$$\begin{aligned}
E_{\text{new}} &= \left(\frac{\epsilon_0 cn}{2}\right)^{\frac{1}{2}} E_{\text{old}}, && (40)\\
q_{\text{new}} &= \frac{2\omega_\nu \epsilon_0 cn}{\tau\gamma} q_{\text{old}}, && (41)\\
g &= \frac{\omega_{-1}\tau\gamma}{4n^2\epsilon_0 c^2\omega_\nu}\chi'^{(3)}, && (42)\\
\kappa_j &= \frac{\omega_j}{c}n_2, && (43)\\
n_2 &= \frac{3}{4cn^2\epsilon_0}\chi^{(3)}, && (44)\\
\Delta k_j &= k_j - k_{j-1} - k_\nu, && (45)\\
\Delta k &= 2k_0 - k_1 - k_{-1}, && (46)
\end{aligned}$$

where g in Eq. (42) is the Raman gain, n_2 in Eq. (44) is the nonlinear refractive index, and k_i ($i = -1, 0, 1$) in Eq. (46) is given as $k_i = \boldsymbol{k}_i \cdot \boldsymbol{z}$, where $\boldsymbol{k}_i \parallel \boldsymbol{z}$ and $\boldsymbol{z}$ is a unit vector in the z direction.

At a steady state, vibrating molecules with a frequency of ω_ν in the employed semiconductor have a constant amplitude for q in the motion of $Q = (qe^{i(k_\nu z - \omega_\nu t)} + \text{c.c.})/2$. Thus, the relation $\partial q/\partial t = 0$ holds, and Eq. (39) gives

$$q = i\left(E_0 E_{-1}^{*} e^{i\Delta k_0 z} + E_1 E_0^{*} e^{i\Delta k_1 z}\right). \tag{47}$$

In this case, substituting Eq. (47) for Eqs. (36)-(38), we obtain

$$\begin{aligned}
\frac{\partial E_{-1}}{\partial z} &= \frac{g}{2}\left(E_0^{*}E_{-1} + E_1^{*}E_0 e^{i\Delta kz}\right)E_0 \\
&\quad + i\kappa_{-1}\left(2|E_0|^2 + |E_{-1}|^2 + 2|E_1|^2\right)E_{-1} + i\kappa_{-1}E_1^{*}E_0^2 e^{i\Delta kz}, &(48)\\
\frac{\partial E_0}{\partial z} &= \frac{g}{2}\frac{\omega_0}{\omega_{-1}}\left(|E_1|^2 - |E_{-1}|^2\right)E_0 \\
&\quad + i\kappa_0\left(|E_0|^2 + 2|E_{-1}|^2 + 2|E_1|^2\right)E_0 + 2i\kappa_0 E_0^{*}E_{-1}E_1 e^{-i\Delta kz}, &(49)\\
\frac{\partial E_1}{\partial z} &= -\frac{g}{2}\frac{\omega_1}{\omega_{-1}}\left(E_0E_{-1}^{*}e^{i\Delta kz} + E_1E_0^{*}\right)E_0 \\
&\quad + i\kappa_1\left(2|E_0|^2 + 2|E_{-1}|^2 + |E_1|^2\right)E_1 + i\kappa_1 E_{-1}^{*}E_0^2 e^{i\Delta kz}. &(50)
\end{aligned}$$

If we include linear-loss terms with a loss coefficient α_j ($j = -1, 0, 1$) and nonlinear-loss terms with a TPA coefficient β_{TPA}, the coupled equations take the form.

$$\begin{aligned}
\frac{\partial E_{-1}}{\partial z} &= \frac{g}{2}\left(E_0^{*}E_{-1} + E_1^{*}E_0 e^{i\Delta kz}\right)E_0 + i\kappa_{-1}\left(2|E_0|^2 + |E_{-1}|^2 + 2|E_1|^2\right)E_{-1} \\
&\quad + i\kappa_{-1}E_1^{*}E_0^2 e^{i\Delta kz} - \frac{1}{2}\left(\alpha_{-1} + \alpha_{-1}^{\mathrm{TPA}}\right)E_{-1}, &(51)\\
\frac{\partial E_0}{\partial z} &= \frac{g}{2}\frac{\omega_0}{\omega_{-1}}\left(|E_1|^2 - |E_{-1}|^2\right)E_0 + i\kappa_0\left(|E_0|^2 + 2|E_{-1}|^2 + 2|E_1|^2\right)E_0 \\
&\quad + 2i\kappa_0 E_0^{*}E_{-1}E_1 e^{-i\Delta kz} - \frac{1}{2}\left(\alpha_0 + \alpha_0^{\mathrm{TPA}}\right)E_0, &(52)\\
\frac{\partial E_1}{\partial z} &= -\frac{g}{2}\frac{\omega_1}{\omega_{-1}}\left(E_0E_{-1}^{*}e^{i\Delta kz} + E_1E_0^{*}\right)E_0 + i\kappa_1\left(2|E_0|^2 + 2|E_{-1}|^2 + |E_1|^2\right)E_1 \\
&\quad + i\kappa_1 E_{-1}^{*}E_0^2 e^{i\Delta kz} - \frac{1}{2}\left(\alpha_1 + \alpha_1^{\mathrm{TPA}}\right)E_1, &(53)
\end{aligned}$$

where α_j^{TPA} is defined by [27, 32]

$$\alpha_j^{\mathrm{TPA}} = \beta_{\mathrm{TPA}}\left(|E_j|^2 + 2\sum_{m\neq j}|E_m|^2\right), \tag{54}$$

and β_{TPA} is defined by

$$\beta_{\mathrm{TPA}} = \frac{3\mu_0\,\omega_j}{2n^2}\chi'^{(3)}. \tag{55}$$

Note that in the above equations, FCA is neglected because the p-n junction in Fig. 1 soon drains off TPA-induced carriers (if there is TPA).

The right-hand side of Eqs. (51)-(53) contains the terms of SRS, SPM, XPM, FWM (degenerate FWM), linear loss, and TPA loss from the left to the right. Here, the terms of SPM, XPM, and FWM are not negligible because the nonlinear coefficient κ_j in Eqs. (51)-(53) is comparable to the Raman gain g for Al$_x$Ga$_{1-x}$As at around 1.55 μm: $g \approx 10$ (cm/GW) [16] and $\kappa_j \approx 7.1$ (cm/GW) [33]. For a comparison, we show g and κ_j of Si at around 1.55 μm: $g \approx 20$ (cm/GW) [4] and $\kappa_j \approx 1.8$ (cm/GW) [34]. For Si, the effect from the SRS terms is much stronger than that from the Kerr terms, which is completely different from the Al$_x$Ga$_{1-x}$As case.

In the next section, we solve Eqs. (51)-(53) by an analytical method with some approximations and also by a numerical method when there is no QPM structure. After checking numerical solutions at the initial evolution stage by comparison with analytical solutions, we proceed to numerically obtain the output efficiency with the QPM structure out of the initial stage.

Note that in what follows, $|E_i|^2$ ($i = -1, 0, 1$) represents an optical intensity in units of GW/cm^2, which is identical to the propagating beam power divided by the waveguide cross-sectional area.

IV. RESULTS AND DISCUSSION

A. Analytical solutions with approximations

To obtain analytical solutions for the coupled nonlinear equations Eqs. (51)-(53), we make the following approximations, which are valid at the initial stage of growth of the Stokes and anti-Stokes waves.

(a) The pump intensity $|E_0|^2$ is sufficiently large compared with the intensities $|E_{-1}|^2$, $|E_1|^2$ of the Stokes and anti-Stokes waves, respectively, where the depletion of the pump beam is neglected. In this case, the condition

$$|E_{-1}|, |E_1| \ll |E_0| = \text{const.} \tag{56}$$

holds. Note that the Stokes and anti-Stokes waves can grow from small seed light and do not necessarily require high-power seed beams at $z = 0$.

(b) Since the anti-Stokes wave with a phase mismatch Δk grows much more weakly than the Stokes wave with no such phase mismatch, an additional approximation

$$|E_1| \ll |E_{-1}| \tag{57}$$

holds.

(c) We ignore the wavelength dependence of the loss coefficients, α_{-1}, α_1, α_0, of the Stokes, anti-Stokes, and pump waves, respectively, because their differences are small at the wavelengths far from the bandgap wavelength (actually they are near the half-bandgap wavelength). In this case, we can set

$$\alpha_{-1} \approx \alpha_1 \approx \alpha_0 \equiv \alpha, \tag{58}$$

where α is a constant.

Employing the above approximations Eqs. (56)-(58), we obtain the following simplified equations for Eqs. (51)-(53):

$$\frac{\partial E_{-1}}{\partial z} \approx \left(\frac{g}{2} - \beta_{\mathrm{TPA}} + 2i\kappa_{-1}\right) |E_0|^2 E_{-1} - \frac{\alpha}{2} E_{-1}, \tag{59}$$

$$\frac{\partial E_1}{\partial z} \approx -\left(\frac{g}{2}\frac{\omega_1}{\omega_{-1}} - i\kappa_1\right) E_0^2 E_{-1}^* \, e^{i\Delta k z} - \frac{\alpha}{2} E_1. \tag{60}$$

In the approximations used above, the effects of SPM and XPM were greatly reduced. (These effects will be examined in detail in §IV B 4.)

In Eqs. (59) and (60), the linear-loss terms are easily removed by setting

$$E_{-1} = \mathcal{E}_{-1}(z)\, e^{-\frac{\alpha}{2}z}, \tag{61}$$

$$E_1 = \mathcal{E}_1(z)\, e^{-\frac{\alpha}{2}z}. \tag{62}$$

We then obtain

$$\frac{\partial \mathcal{E}_{-1}}{\partial z} \approx \left(\frac{g}{2} - \beta_{\mathrm{TPA}} + 2i\kappa_{-1}\right) |E_0|^2\, \mathcal{E}_{-1}, \tag{63}$$

$$\frac{\partial \mathcal{E}_1}{\partial z} \approx -\left(\frac{g}{2}\frac{\omega_1}{\omega_{-1}} - i\kappa_1\right) E_0^2\, \mathcal{E}_{-1}^* \, e^{i\Delta k z}. \tag{64}$$

To solve Eqs. (63) and (64), we integrate Eq. (63) from 0 to z and get

$$\mathcal{E}_{-1}(z) = \mathcal{E}_{-1}(0)\, e^{\left(\frac{g}{2}-\beta_{\rm TPA}+2i\kappa_{-1}\right)|E_0|^2 z}. \tag{65}$$

Next, inserting Eq. (65) into Eq. (64) and integrating Eq. (64) from 0 to z, we obtain

$$\mathcal{E}_1(z) = \mathcal{E}_1(0) + \left(\frac{g}{2}\frac{\omega_1}{\omega_{-1}} - i\kappa_1\right) E_0^2\, \mathcal{E}_{-1}^*(0)\, \frac{1 - e^{\left\{\left(\frac{g}{2}-\beta_{\rm TPA}\right)|E_0|^2 + i\left(\Delta k - 2\kappa_{-1}|E_0|^2\right)\right\}z}}{\left(\frac{g}{2}-\beta_{\rm TPA}\right)|E_0|^2 + i\left(\Delta k - 2\kappa_{-1}|E_0|^2\right)}, \tag{66}$$

where $\mathcal{E}_1(0)$ denotes the input electric field for the anti-Stokes wave. In what follows, we set $\mathcal{E}_1(0) \approx 0$ as $\mathcal{E}_1(0)$ being a very small quantity.

Finally, substituting Eqs. (65) and (66) for Eqs. (61) and (62), we obtain

$$E_{-1}(z) = E_{-1}(0)\, e^{\left\{\left(\frac{g}{2}-\beta_{\rm TPA}+2i\kappa_{-1}\right)|E_0|^2 - \frac{\alpha}{2}\right\}z}, \tag{67}$$

$$E_1(z) = \left(\frac{g}{2}\frac{\omega_1}{\omega_{-1}} - i\kappa_1\right) E_0^2\, E_{-1}^*(0)\, e^{-\frac{\alpha}{2}z} \frac{1 - e^{\left\{\left(\frac{g}{2}-\beta_{\rm TPA}\right)|E_0|^2 + i\left(\Delta k - 2\kappa_{-1}|E_0|^2\right)\right\}z}}{\left(\frac{g}{2}-\beta_{\rm TPA}\right)|E_0|^2 + i\left(\Delta k - 2\kappa_{-1}|E_0|^2\right)}, \tag{68}$$

where the relations $E_1(0) = \mathcal{E}_1(0)$, $E_{-1}(0) = \mathcal{E}_{-1}(0)$ were used. From Eqs. (67) and (68), the output efficiencies, $\eta_{\rm S} = |E_{-1}(z)|^2/|E_0|^2$, $\eta_{\rm AS} = |E_1(z)|^2/|E_0|^2$ (i.e., the z-dependent Stokes and anti-Stokes intensities, $|E_{-1}(z)|^2, |E_1(z)|^2$, divided by the initial pump intensity $|E_0(0)|^2 = |E_0|^2$) are given as follows:

$$\eta_{\rm S} = \frac{|E_{-1}(0)|^2}{|E_0|^2}\, e^{\left\{(g-2\beta_{\rm TPA})|E_0|^2 - \alpha\right\}z}, \tag{69}$$

$$\begin{aligned} \eta_{\rm AS} = {} & \left(\frac{g^2}{4}\frac{\omega_1^2}{\omega_{-1}^2} + \kappa_1^2\right)|E_0|^2|E_{-1}(0)|^2\, e^{-\alpha z} \\ & \times \frac{1 - 2\cos\left(\left(\Delta k - 2\kappa_{-1}|E_0|^2\right)z\right) e^{\left(\frac{g}{2}-\beta_{\rm TPA}\right)|E_0|^2 z} + e^{(g-2\beta_{\rm TPA})|E_0|^2 z}}{\left(\frac{g}{2}-\beta_{\rm TPA}\right)^2|E_0|^4 + \left(\Delta k - 2\kappa_{-1}|E_0|^2\right)^2}. \end{aligned} \tag{70}$$

From Eqs. (69) and (70), we can see some properties on the evolution of the Stokes and anti-Stokes waves:

(i) SRS and TPA for both Stokes and anti-Stokes waves in Eqs. (69) and (70) have the same dependence on the pump intensity $|E_0|^2$, which originates from the property that their coefficients g, $\beta_{\rm TPA}$ have the same origin of $\chi'^{(3)}$, as seen in Eqs. (42) and (55), and have the same unit (cm/GW).

(ii) In addition to the linear optical loss ($e^{-\alpha z}$), SRS for the Stokes wave is suppressed by TPA as $e^{(g-2\beta_{\rm TPA})|E_0|^2 z}$, as seen in Eq. (69). For the anti-Stokes wave in Eq. (70), SRS with optical losses is seemingly complicated because of the presence of Δk in Eq. (70). But the basic feature is that, in addition to the linear loss ($e^{-\alpha z}$), SRS with $e^{g|E_0|^2 z}$ is suppressed by TPA with $e^{-\beta_{\rm TPA}|E_0|^2 z}$, resulting in $e^{(g-2\beta_{\rm TPA})|E_0|^2 z}$ and $e^{(g/2-\beta_{\rm TPA})|E_0|^2 z}$.

(iii) The output efficiency of the anti-Stokes wave in Eq. (70) oscillates with a period of $\Lambda' = 2\pi/|\Delta k - 2\kappa_{-1}|E_0|^2|$ that depends on $2\kappa_{-1}|E_0|^2$. Thus the period has an $|E_0|^2$-dependence.

(iv) The output efficiency of the anti-Stokes wave in Eq. (70) is enhanced by an additional factor κ_1^2 that stems from FWM, which is added to the SRS factor $(g^2/4)(\omega_1^2/\omega_{-1}^2)$.

As regards (i), since g and $\beta_{\rm TPA}$ are proportional to $\chi'^{(3)}$, as seen in Eqs. (42) and (55), and since n_2 is proportional to $\chi^{(3)}$, as seen in Eq. (44), these coefficients in the intermixed domains are smaller than those in the as-grown domains because of blue-shifted resonance for $\chi^{(3)}$ and $\chi'^{(3)}$. Thus, periodic g and n_2 are produced in the GaAs/AlAs-intermixed-superlattice waveguide. These periodic g and n_2 form the QPM structure that can remove Δk and enhance the output efficiency.

In connection with (ii), if the photon energies of the Stokes and anti-Stokes waves are smaller than the half-bandgap energy, TPA that degrades SRS can be greatly reduced. Even in this region, n_2 has a finite value (and becomes large near the half-bandgap energy) [28]. For this reason, we use a semiconductor device with the photon energies of the pump, Stokes, and anti-Stokes waves near and below the half-bandgap energy for highly-efficient output (or with their wavelengths near and larger than the half-bandgap wavelength).

In relation to (iii), the setting of the QPM period Λ to $\Lambda' = 2\pi/|\Delta k - 2\kappa_{-1}|E_0|^2|$ is not practical in device applications, because $|E_0|^2$ actually decreases as the pump wave propagates through the QPM device, as will be shown in §IV B, which requires an aperiodic QPM structure. In addition, $|E_0|^2$ at $z = 0$ is sometimes varied, and a corresponding aperiodic QPM structure is necessary in this case. This means that there is no availability for a wide change in input pump intensity. For this reason, we set $\Lambda = 2\pi/|\Delta k|$ when performing QPM.

With respect to (iv), because of $\kappa_1^2 \approx 50.4$ and $(g^2/4)(\omega_1^2/\omega_{-1}^2) \approx 29.9$ in our case, we can see that the FWM-enhanced efficiency is about 2.7 times greater than that without FWM. For a comparison, we here mention that Si has $\kappa_1^2 \approx 3.3$ and $(g^2/4)(\omega_1^2/\omega_{-1}^2) \approx 119.6$, which means that Si has a little efficiency enhancement by FWM. On the other hand, such an enhancement has been reported in an optical fiber (SiO_2) with no QPM structure [35]. However, our device has a QPM structure, and we need to investigate the effect of SRS with FWM on QPM. At the same time, we need to take account of SPM and XPM, which are much stronger than those in SiO_2 as well as in Si. The numerical analysis containing all those effects on the efficiency is given in the next section.

B. Numerical solutions

The solutions in §IV A with approximations for nonlinear optical terms did not contain the effects of pump depletion and very large growth of the Stokes wave under the assumption that they were at the initial stage. To investigate the evolution of the three waves more precisely, we obtain numerical solutions (i.e., without such approximations) for the case without QPM at first by the fourth-order Runge-Kutta method [36]. At the initial wave evolution, since those two effects are not serious, a comparison between the analytical and numerical solutions can be made to check numerical accuracy, which will be described in §IV B 4. After this check, we proceed to investigate the solutions for the case with QPM, and show improved output characteristics in comparison with no QPM case.

1. Determination of the half-bandgap, Stokes, pump, and anti-Stokes wavelengths

We have used $Al_xGa_{1-x}As$ ($x = 0.18$), where the $\chi^{(3)}$-property of the as-grown GaAs/AlAs superlattice can be well approximated. These two have quite a similar $\chi^{(3)}$-property and almost the same bandgap energy [28]. We do not have to focus on TPA in the intermixed regions because they have a blue-shifted absorption edge and TPA in the as-grown regions emerges at first. In this superlattice, we have assumed that the Stokes, pump, and anti-Stokes wavelengths, λ_i $(i = -1, 0, 1)$, respectively, are near and larger than the half-bandgap wavelength λ_{half}, thus keeping large n_2 and very small (almost zero) β_{TPA}. (Here, a large figure of merit, $4\pi n_2/(\beta_{\text{TPA}}\lambda_i) \gg 1$, is kept even at $\lambda_i = \lambda_{\text{half}}$ [37, 38].)

To show available λ_{-1}, λ_0, λ_1, we need to calculate λ_{half} (μm) that is defined by

$$\lambda_{\text{half}} = 2\frac{hc}{E_{\text{g}}}, \tag{71}$$

where h is Planck's constant, c is the velocity of light, and E_{g} (eV) is the bandgap energy at a temperature of T (K). E_{g} in Eq. (71) can be determined from Varshni's equation [39] for $\text{Al}_x\text{Ga}_{1-x}\text{As}$.

$$E_{\text{g}} = E_{\text{g}}^{(0)} - \frac{aT^2}{b+T}, \tag{72}$$

where $E_{\text{g}}^{(0)} = 1.5194 + 1.36\,x + 0.22\,x^2$ (eV) $(0.1 < x < 0.75)$ [40], $a = (5.5 + 3.35\,x)\,10^{-4}$ (eV/K), and $b = 225 + 88\,x$ (K) $(0 < x < 0.7)$ that are valid for 12 - 800 K [41].

Setting $x = 0.18$ and $T = 300$ K (room temperature) in Eqs. (71) and (72), we obtain $E_{\text{g}} = 1.67$ eV and $\lambda_{\text{half}} = 1.485$ μm. Thus, as λ_{-1}, λ_0, and λ_1 near and larger than $\lambda_{\text{half}} = 1.485$ μm (0.835 eV), we obtain $\lambda_{-1} = 1.63$ μm (0.761 eV), $\lambda_0 = 1.56$ μm (0.795 eV), and $\lambda_1 = 1.49$ μm (0.832 eV). Here, the spacing of λ_{-1}, λ_0, λ_1 was determined from the Raman shift (70.8 nm) of $\text{Al}_x\text{Ga}_{1-x}\text{As}$.

2. Determination of the phase mismatch Δk

It is also necessary to determine the phase mismatch Δk in Eqs. (51)-(53) when performing the numerical integration of them. This Δk is defined by

$$\Delta k = 2k_0 - k_1 - k_{-1} = 2\pi\left(2\frac{n(\lambda_0)}{\lambda_0} - \frac{n(\lambda_1)}{\lambda_1} - \frac{n(\lambda_{-1})}{\lambda_{-1}}\right), \tag{73}$$

where $n(\lambda_i)$ is the refractive index for λ_i $(i = -1, 0, 1)$. The form of $n(\lambda_i)$ is determined by Sellmeier's equation for $\text{Al}_x\text{Ga}_{1-x}\text{As}$ at room temperature [42, 43], which is given by

$$n(\lambda_i) = \left\{a_1 - a_2\,x + \frac{a_3}{\lambda_i^2 - (a_4 - a_5\,x)^2} - a_6\,(a_7\,x + 1)\,\lambda_i^2\right\}^{\frac{1}{2}}, \tag{74}$$

where for $x \leq 0.36$, $a_1 = 10.906$, $a_2 = 2.92$, $a_3 = 0.97501$, $a_4 = 0.52886$, $a_5 = 0.735$, $a_6 = 0.002467$, and $a_7 = 1.41$. For $x > 0.36$, a_4 and a_5 are changed to $a_4 = 0.30386$ and $a_5 = 0.105$. Since Sellmeier's equation for the as-grown regions has not been obtained, although there have been some experimentally measured data of refractive indices at around 1.55 μm [23], we use Eq. (74) with $x = 0.18$ as an approximate refractive index for the as-grown regions. When compared with the experimentally measured refractive index at 1.55 μm for TE modes [23], the deviation of the refractive index from that in Eq. (74) with $x = 0.18$ at 1.55 μm is 5.8 %.

From Eqs. (73) and (74), we can determine the QPM period Λ for first-order QPM as $\Lambda = 2\pi/|\Delta k|$. By inserting $\lambda_{-1} = 1.63$ μm, $\lambda_0 = 1.56$ μm, and $\lambda_1 = 1.49$ μm into Eqs. (73) and (74), we obtain $\Lambda = 189.1\mu$m.

3. *Determination of the linear loss coefficient α*

Since the Stokes, pump, and anti-Stokes wavelengths are larger than the half-bandgap wavelength, the TPA loss does not emerge, but the linear loss emerges at all times. However, recent technological development has achieved a small linear loss, e.g., a loss of 1.2 dB/cm in $\mathrm{Al}_x\mathrm{Ga}_{1-x}\mathrm{As}$ ($x = 0.18$) at around 1.55 μm for TE-mode beams [44]. In our calculations, we employ this value. In addition, since the wavelengths larger than the half-bandgap wavelength are far from the bandgap wavelength, we can justify the omission of the wavelength dependence of the linear-loss coefficients α_j ($j = -1, 0, 1$), as given in Eq. (58), and we set $\alpha_j = \alpha = 0.276$ cm^{-1}. This was calculated from the loss of 1.2 dB/cm so as to fit $e^{-\alpha z}$.

4. *Output efficiencies for the cases with and without QPM*

Using the above phase mismatch Δk, the refractive indices $n(\lambda_i)$ of the above wavelengths λ_i ($i = -1, 0, 1$), the linear loss coefficient α, and the numerical factors of g and κ_j given in §III D, we numerically compute the output efficiencies, $\eta_{\mathrm{S}} = |E_{-1}(z)|^2/|E_0(0)|^2$, $\eta_{\mathrm{AS}} = |E_1(z)|^2/|E_0(0)|^2$, for the cases with and without QPM.

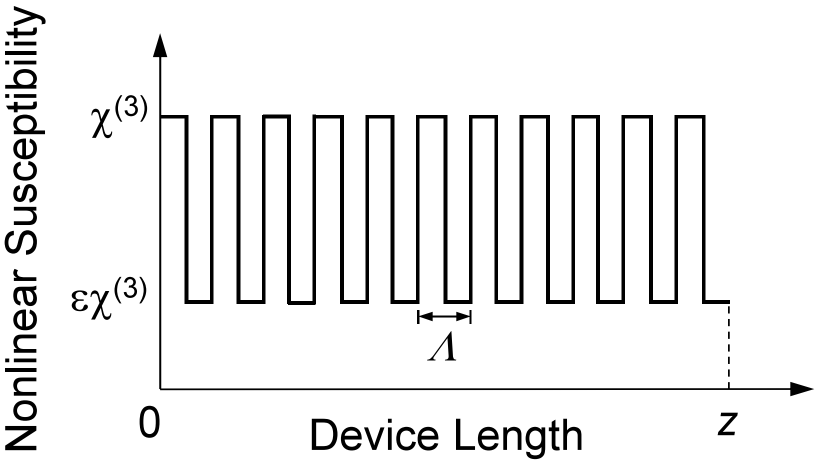

FIG. 3. Third-order nonlinear susceptibility $\chi^{(3)}$ change in the QPM structure. $\chi^{(3)}$ in the intermixed domains is set to $\varepsilon\chi^{(3)}$ with $0 \leq \varepsilon \leq 1$. Λ is a QPM period.

In numerical calculations with QPM, a small difference between the refractive indices, $n_{\mathrm{intermixed}}$ and $n_{\mathrm{as-grown}}$, in the intermixed and as-grown domains, respectively, is ignored because the difference $n_{\mathrm{as-grown}} - n_{\mathrm{intermixed}} = 0.01$ is only 0.3 % of the average refractive index of the QPM structure, as already mentioned in §I. On the other hand, a large change in $\chi^{(3)}$ of the intermixed domains is set as $\varepsilon\chi^{(3)}$ $(0 \leq \varepsilon \leq 1)$ using the $\chi^{(3)}$ of the as-grown domains, as depicted in Fig. 3. This setting means that when $\varepsilon = 1$, there is no QPM structure and that when $0 \leq \varepsilon < 1$, there is a QPM structure. In particular, $\varepsilon = 0$ gives a maximum QPM effect.

To calculate the output efficiencies, we use a waveguide with a cross-sectional area of (0.5 μm)^2 and with a pump power of 10 W [45] that can be achieved with fiber lasers. In this case, the pump intensity at $z = 0$ is $|E_0(0)|^2 = 4.0$ (GW/cm^2). As seed-light intensities at $z = 0$ for the Stokes and anti-Stokes waves, we tentatively set $|E_{-1}(0)|^2 = 0.01$ (GW/cm^2) and $|E_1(0)|^2 = 0.0001$ (GW/cm^2). Note that the setting of $|E_{-1}(0)|^2 \approx |E_1(0)|^2 = 0.01$ (GW/cm^2) is possible. But we numerically checked that within $0.0001 \leq |E_1(0)|^2 \leq 0.01$ (GW/cm^2), there was no noticeable change in the growth of the Stokes and anti-Stokes waves. Why we set $|E_0(0)|^2 = 4.0$ (GW/cm^2) $\gg |E_{-1}(0)|^2 = 0.01$ (GW/cm^2) $\gg |E_1(0)|^2 = 0.0001$ (GW/cm^2) is that this enables comparing numerical results to the analytical results

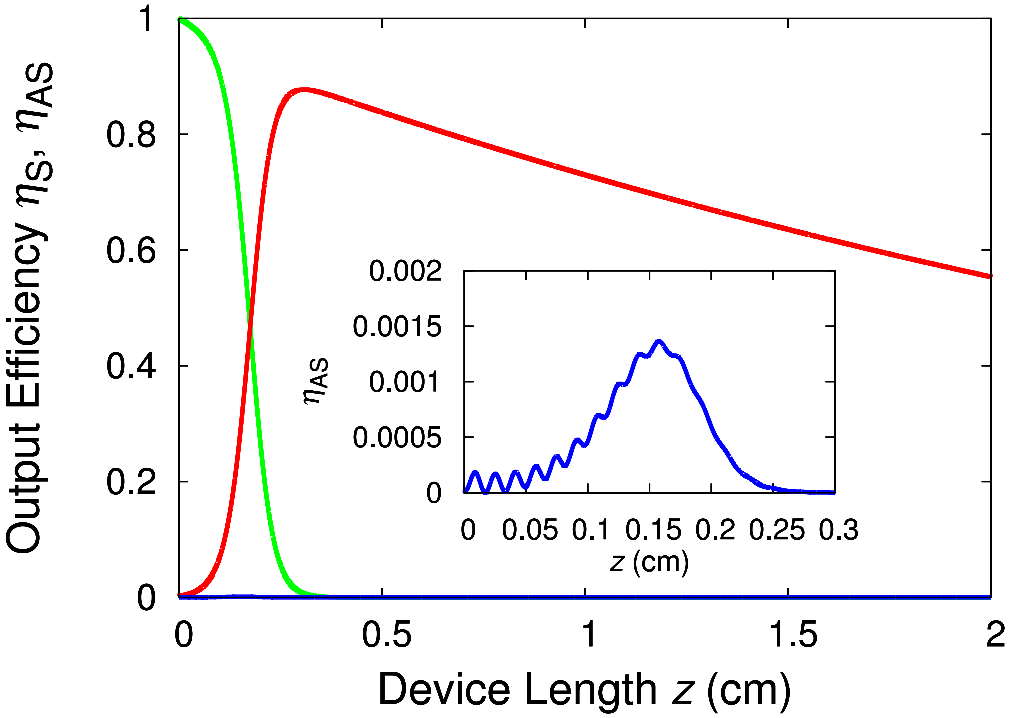

FIG. 4. Output efficiencies $\eta_S = |E_{-1}(z)|^2/|E_0(0)|^2$, $\eta_{AS} = |E_1(z)|^2/|E_0(0)|^2$ of the Stokes and anti-Stokes waves, respectively, for $\varepsilon = 1$ (i.e., without QPM). The red and blue curves indicate η_S and η_{AS}, respectively, and the green curve indicates the normalized pump intensity $|E_0(z)|^2/|E_0(0)|^2$. The inset depicts a magnified figure of η_{AS} at around 0.15 cm.

with the approximations in Eqs. (56) and (57).

The output efficiencies η_S, η_{AS} for $\varepsilon = 1$ (i.e., without QPM) as a function of the device length z are shown in Fig. 4, indicated by the red and blue curves, respectively. The pump intensity $|E_0(z)|^2$ divided by $|E_0(0)|^2$ was also added to Fig. 4, indicated by the green curve, which shows a rapid decrease with increasing z. The inset of Fig. 4 is a magnified figure of η_{AS} at around $z = 0.15$ cm, which shows that η_{AS} oscillates and does not grow sufficiently due to a non-zero phase mismatch Δk and pump depletion. In this case, most of the pump power is transferred to the Stokes wave that has no such phase mismatch.

From the inset of Fig. 4, we can roughly estimate the ratio, $|E_1|^2/|E_{-1}|^2$, between the anti-Stokes-wave and Stokes-wave intensities to be 10^{-3}, which is rather larger than 10^{-5} - 10^{-6} in Si waveguides [18, 19]. This comes from $|E_1|^2/|E_{-1}|^2$ proportional to the pump intensity $|E_0|^2$ [17] with the use of a larger $|E_0|^2$ in our case.

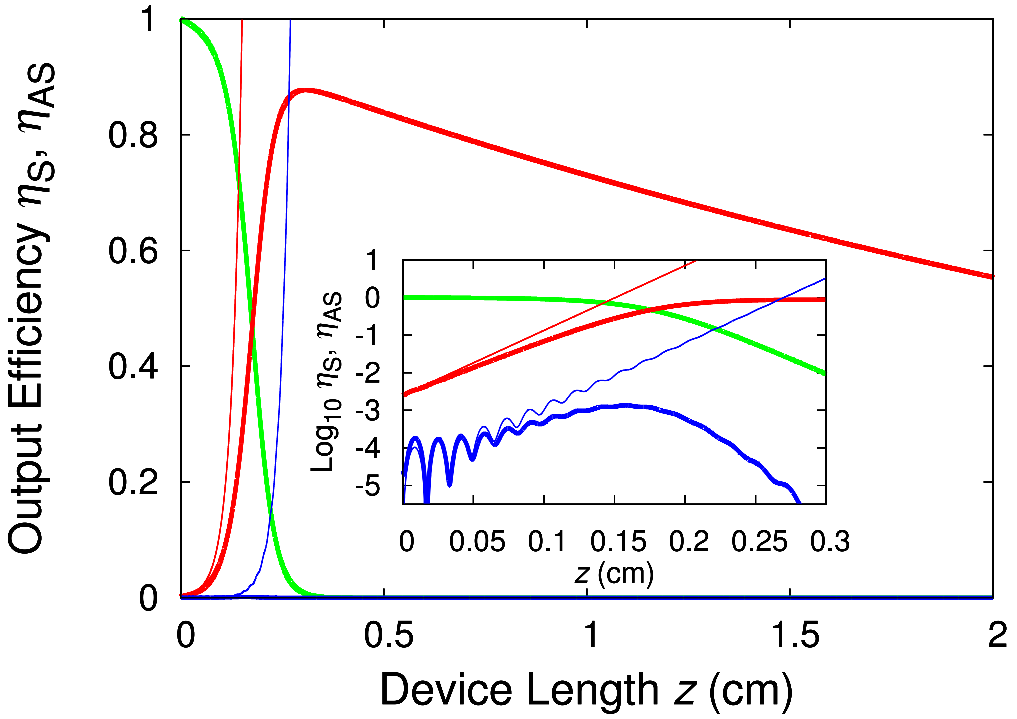

FIG. 5. Comparison between analytical and numerical results, indicated by the thin and thick curves, respectively, where the thick curves are the same as in Fig. 4. The inset shows the same figure with the $\log_{10}$ plot of the vertical axis.

As mentioned above, the input intensity setting in numerical calculations that satisfies $|E_0| \gg |E_{-1}| \gg |E_1|$ enables comparing the numerical results with the analytical solutions in Eqs. (69) and (70) when $\beta_{\mathrm{TPA}} = 0$. This is shown in Fig. 5, where the thin red and blue curves express those of Eqs. (69) and (70), respectively, and the thick red, blue, and green curves are the same as in Fig. 4. The inset displays the same figure with the $\log_{10}$ plot for the vertical axis. We observe that at the initial stage of growth of the Stokes and anti-Stokes waves, the numerical solutions well fit the analytical results but that as z increases, they deviate from the analytical results. The main cause of this is pump depletion, and there is also another effect from SPM and XPM that are greatly reduced in the approximations for the analytical solutions. The latter effect will be described below (see Fig. 7).

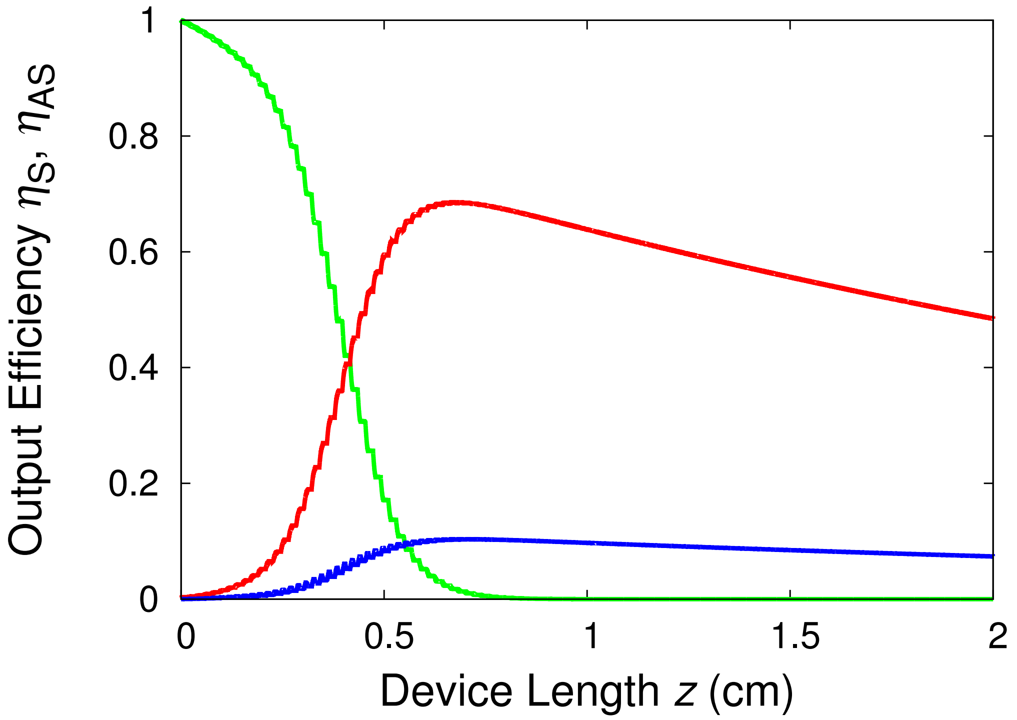

FIG. 6. Output efficiencies $\eta_{\rm S}$, $\eta_{\rm AS}$ of the Stokes and anti-Stokes waves, respectively, for $\varepsilon = 0$ (i.e., with QPM giving the maximum efficiency). The red and blue curves show $\eta_{\rm S}$ and $\eta_{\rm AS}$, respectively, and the green curve indicates the normalized pump intensity.

Figure 6 shows the output efficiencies $\eta_{\rm S}$, $\eta_{\rm AS}$ for $\varepsilon = 0$ (i.e., with QPM that provides the maximum efficiency), where we observe a great increase in $\eta_{\rm AS}$ due to QPM, which reaches the same order of $\eta_{\rm S}$ (but with a factor of about 1/7). In addition, we can see that there is an optimal device length that provides the highest efficiency in $\eta_{\rm AS}$ at $z_{\rm peak} = 0.69$ cm that is determined from a balance between optical gain and loss. This gives us useful information on determining a necessary device length when we fabricate actual devices. In this case, $\eta_{\rm S}$ of the Stokes wave somewhat decreases because more pump power is transferred to the anti-Stokes power. We also checked the influence of an initial phase shift (i.e., at $z = 0$) of the QPM period on $\eta_{\rm AS}$, and observed very little effect on it.

To check the effects of SPM and XPM on SRS of the anti-Stokes wave including FWM, we depict $\eta_{\rm AS}$ when SPM and/or XPM effects are deliberately deleted. The black curve in

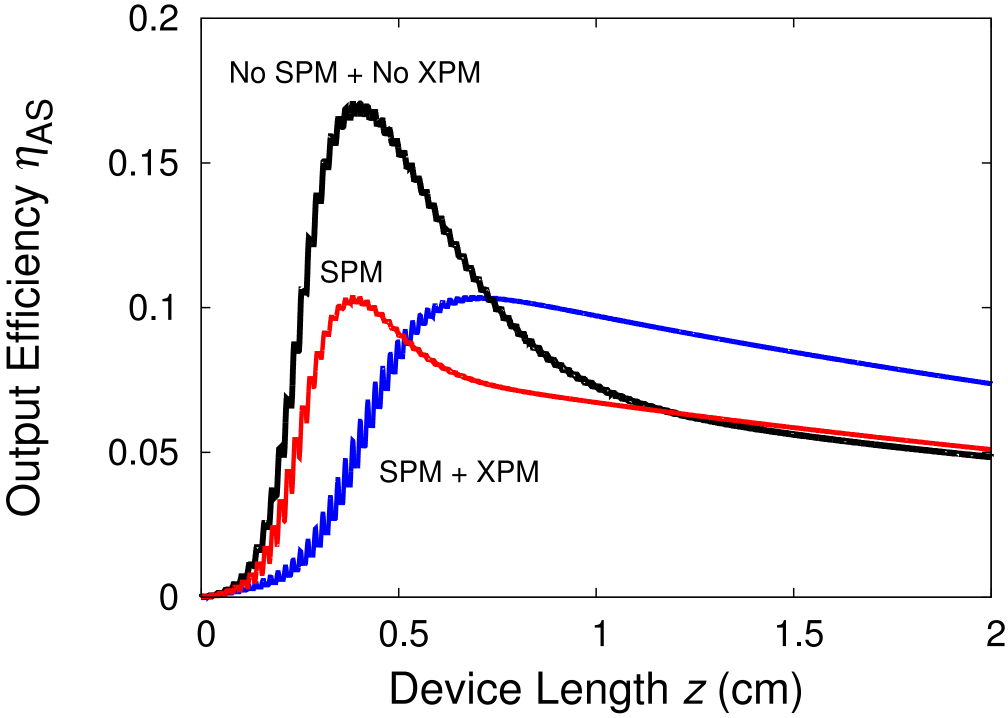

FIG. 7. Output efficiency $\eta_{\rm AS}$ without SPM and XPM, indicated by the black curve. The blue curve shows the case when SPM and XPM are included. The red curve indicates the case when only SPM is taken into account.

Fig 7 depicts $\eta_{\rm AS}$ when only SRS and FWM are taken into account. The blue curve shows $\eta_{\rm AS}$ containing both SPM and XPM effects, which is the same as that in Fig. 6.

In the black curve, we can see that QPM is more effective because there is no period deviation from $\Lambda = 2\pi/|\Delta k|$ by a phase shift due to SPM and XPM. Owing to this effective QPM, $\eta_{\rm AS}$ grows more rapidly than that with SPM and XPM as the anti-Stokes wave propagates in the z direction; in this case, about 1.6 times larger $\eta_{\rm AS}$ is obtained at $z = 0.4$ cm.

Furthermore, in order to see only the SPM effect on $\eta_{\rm AS}$, we intentionally delete the XPM effect, as depicted in Fig. 7 by the red curve. We can see that this also causes a period deviation from $\Lambda = 2\pi/|\Delta k|$, thus decreasing $\eta_{\rm AS}$. But, in our semiconductor device, since we cannot remove only SPM and/or XPM effects in an artificial manner, the device cannot get rid of the efficiency reduction.

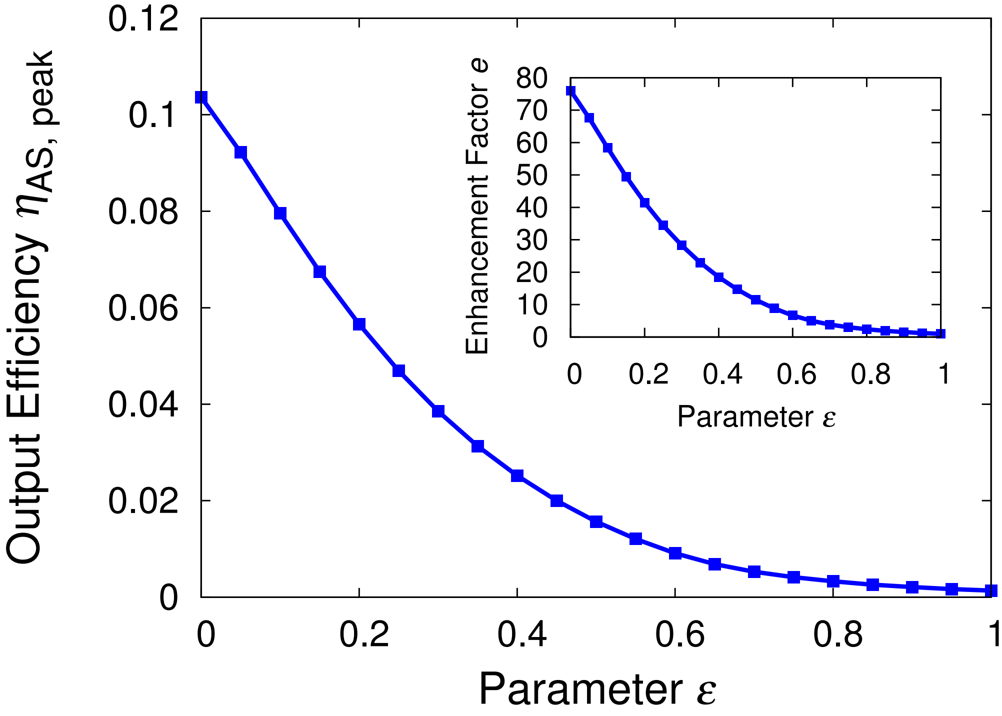

FIG. 8. Output efficiency η_{AS} at $z = z_{\mathrm{peak}}$ as a function of ε ($0 \leq \varepsilon \leq 1$). The inset depicts the enhancement factor e.

Next, we check the dependence of η_{AS} on the parameter ε ($0 \leq \varepsilon \leq 1$) while taking account of all the above nonlinear effects. Figure 8 shows the peak value of η_{AS} at $z = z_{\mathrm{peak}}$, denoted by $\eta_{\mathrm{AS,peak}}$, as a function of ε. In Fig. 8, we can see that as ε approaches 0 from 1, $\eta_{\mathrm{AS,\,peak}}$ increases rapidly. To obtain an enhancement factor e (or figure of merit) due to QPM when compared with that without QPM (i.e., $\varepsilon = 1$), we calculate the enhancement factor e defined by

$$e = \frac{\eta_{\mathrm{AS,\,peak,}\,\varepsilon}}{\eta_{\mathrm{AS,\,peak,}\,\varepsilon=1}} = \frac{|E_1|^2_{\mathrm{peak,}\,\varepsilon}}{|E_1|^2_{\mathrm{peak,}\,\varepsilon=1}}. \tag{75}$$

This is depicted in the inset of in Fig. 8, which shows that e is about 76 times greater at $\varepsilon = 0$ (with the maximum QPM effect) than that at $\varepsilon = 1$ (with no QPM effect). Since the actually-achievable value of ε is ~ 0.5 [28], the enhancement factor e in this case is ~ 11.5.

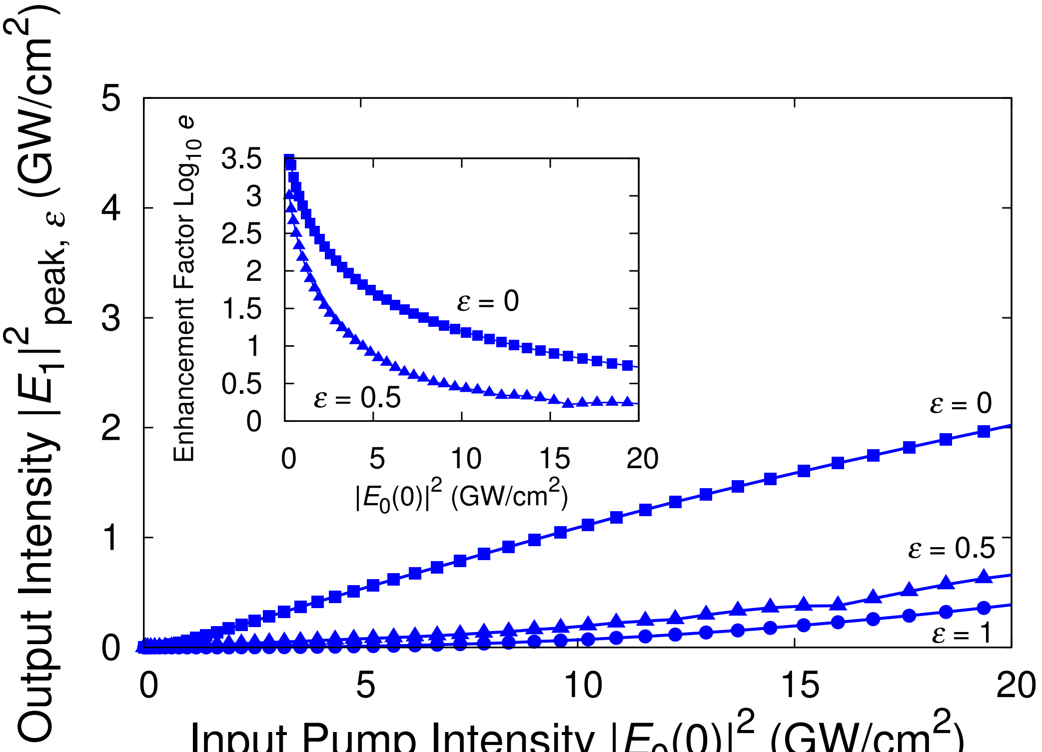

FIG. 9. Dependence of peak output intensity $|E_1|^2_{\text{peak},\varepsilon}$ on the input pump intensity $|E_0(0)|^2$ for $\varepsilon = 0, 0.5, 1$. The inset depicts the $\log_{10}$ plot of the enhancement factor e that depends on $|E_0(0)|^2$ when $\varepsilon = 0, 0.5$.

The enhancement factor e in the inset of Fig. 8 was obtained when the initial pump intensity $|E_0(0)|^2$ was fixed at 4.0 (GW/cm^2). As we can easily see, an increase in the initial pump intensity $|E_0(0)|^2$ increases the anti-Stokes-wave intensity $|E_1|^2_{\text{peak},\varepsilon}$, which is shown in Fig. 9. Thus our interest now goes to the dependence of e on $|E_0(0)|^2$.

The dependence of e on $|E_0(0)|^2$ is depicted in the inset of Fig. 9, where the vertical axis is set on a $\log_{10}$ scale. This shows that e takes a very large value between 10^3 and $10^{3.5}$ for $0 \leq \varepsilon \leq 0.5$ at very small $|E_0(0)|^2$, where $|E_0(0)|^2$ should be larger than the SRS threshold pump intensity $\delta \approx 10^{-2}$ (GW/cm^2) [46]. The increase in e originates from the cause that as $|E_0(0)|^2$ approaches δ, the intensity-dependent period $\Lambda' = 2\pi/|\Delta k - 2\kappa_{-1}|E_0|^2|$ in (iii) of §IV A comes nearer to $\Lambda = 2\pi/|\Delta k|$, thereby achieving highly-efficient QPM. Note that the above Λ' will actually be affected by not only SPM but also XPM at the region beyond the approximations of §IV A. But actually, both SPM and XPM simultaneously diminish as $|E_0(0)|^2$ approaches δ, and thus the above simple interpretation holds in explaining the e-enhancement.

For a comparison, in the perfectly-phase-matched case (i.e., $\Delta k = 0$), we can calculate the enhancement factor $e' = \eta_{\rm AS}(\Delta k = 0)/\eta_{\rm AS}(\Delta k \neq 0)$ from Eq. (70) and obtain $e' \gtrsim 5.9 \times 10^3 \approx 10^{3.77}$ for $|E_0|^2 \approx 0$ with $z \gtrsim 0.35$ cm (where 0.35 cm appears because of $z_{\rm peak} > 0.35$ cm at $|E_0|^2 < 4$ (GW/cm^2) for $\varepsilon \leq 0.5$, as will be shown in Fig. 10). This estimation indicates that the above e-enhancement between 10^3 and $10^{3.5}$ is very large and yet still smaller than that in the perfectly-phase-matched case.

6. *Dependence of peak position on the pump intensity*

In actual device fabrication, it is important to determine an optimal (i.e., the smallest) device length that gives the highest output intensity. Figure 10 depicts the dependence of the optimal device length $z_{\rm peak}$ on the pump intensity $|E_0(0)|^2$, which shows that $z_{\rm peak}$ decreases as $|E_0(0)|^2$ increases. This is because as $|E_0(0)|^2$ increases, the Stokes and anti-Stokes waves grow rapidly, thus causing rapid pump depletion. After complete pump depletion, the Stokes and anti-Stokes waves do not grow and are attenuated by the linear optical loss. Thus $z = z_{\rm peak}$ is given approximately from the complete-pump-depletion point.

The important information obtained from Fig. 10 is that we can determine the lower limit of an input pump intensity $|E_0(0)|^2$ for the optimal waveguide length; For instance, as shown in the inset of Fig. 10 by the dashed line for $\varepsilon = 0.5$, $|E_0(0)|^2 = 1.2$ (GW/cm^2) is necessary such that $z_{\rm peak} = 1$ (cm) that is the length aiming to actual device fabrication.

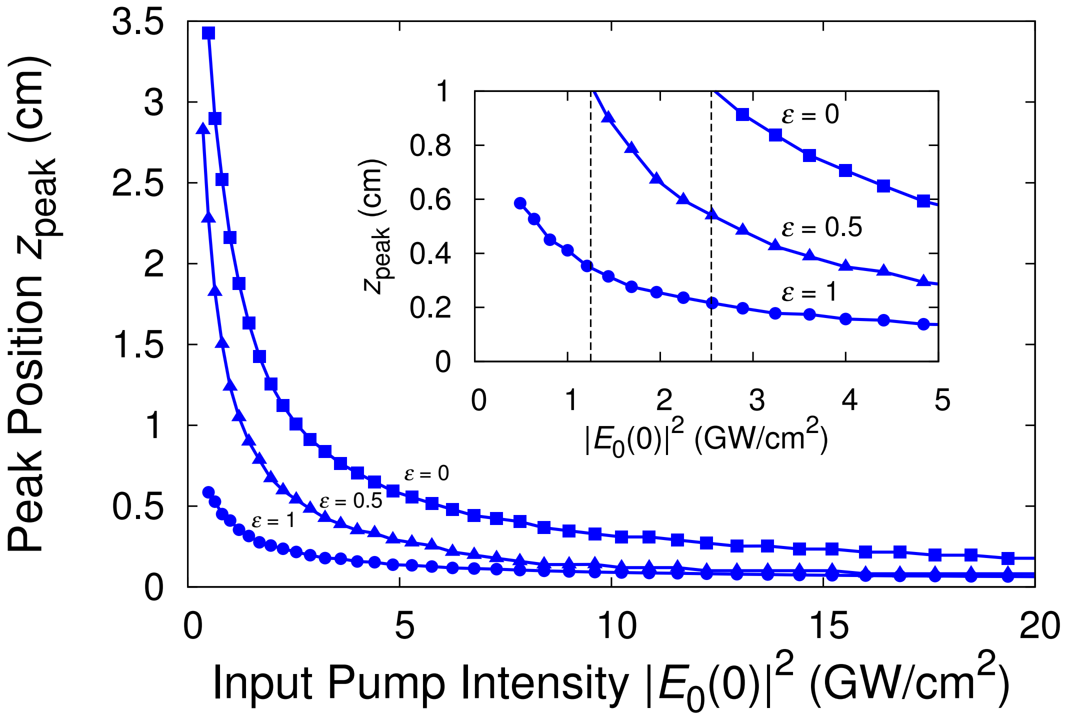

FIG. 10. Dependence of the peak position z_{peak} on the input pump intensity $|E_0(0)|^2$ for $\varepsilon = 0, 0.5, 1$. The inset shows a magnified figure for the range of $0 \leq z_{\text{peak}} \leq 1$ (cm) and $0 < |E_0(0)|^2 < 5$ (GW/cm^2). The dashed lines indicate the necessary $|E_0(0)|^2$ for $z_{\text{peak}} = 1$ (cm) when $\varepsilon = 0, 0.5$.

7. *Dependence of output efficiency on TPA*

In §IV B 1, since the Stokes, pump, and anti-Stokes wavelengths, λ_i ($i = -1, 0, 1$), respectively, were near and larger than the half-bandgap wavelength, λ_{half}, sizable n_2 and negligibly small β_{TPA} were obtained (i.e., high nonlinear refraction and very small TPA). But, in case of smaller λ_i ($i = -1, 0, 1$) than λ_{half}, TPA will emerge strongly. We will examine this effect on the output efficiency.

TPA excites carriers, which give rise to FCA, i.e., an additional optical absorption. But we can remove this additional absorption by use of the reversed-biased p-n junction in Fig. 1.

A detailed calculation containing FCA, e.g., in a Si waveguide, shows a remarkable increase in the optical losses of propagating beams with increasing input beam power, that is, the influence of FCA is far greater than that of only TPA [47]. Thus, the removal of

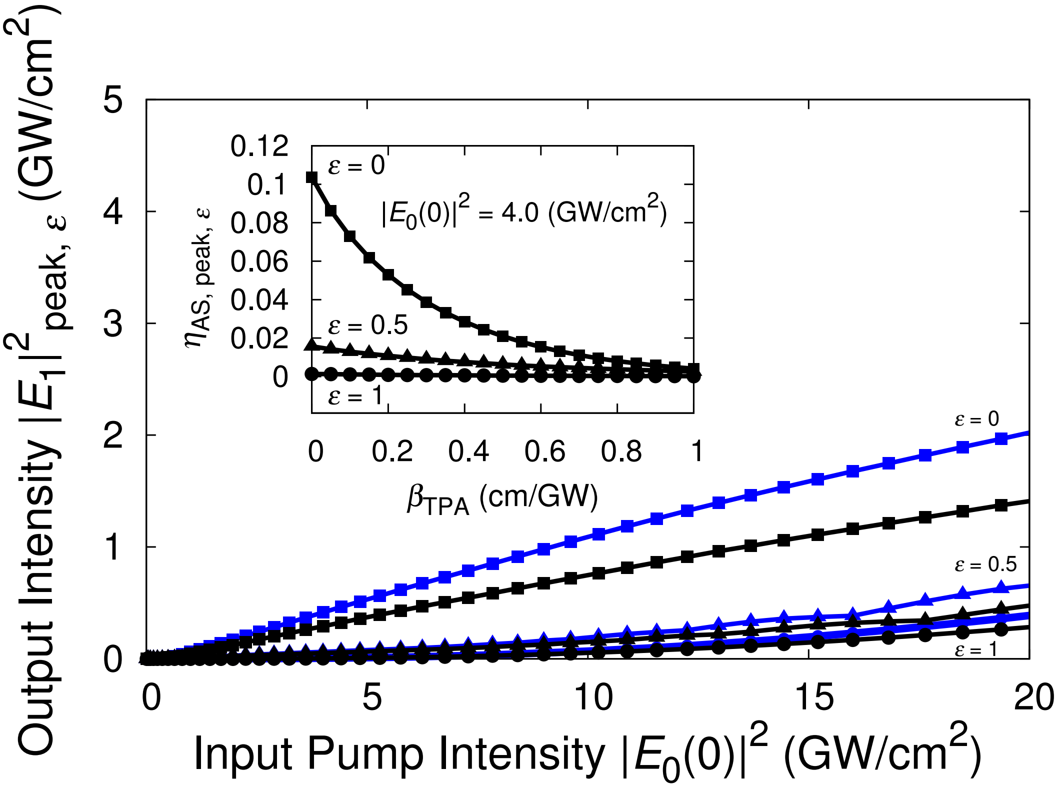

FIG. 11. Input pump intensity $|E_0(0)|^2$-dependence of the peak output intensity $|E_1|^2_{\text{peak},\varepsilon}$ of the anti-Stokes wave for $\varepsilon = 0, 0.5, 1$ with $\beta_{\text{TPA}} = 0.1$ (cm/GW), indicated by the black curves, and with $\beta_{\text{TPA}} = 0$ (cm/GW), indicated by the blue curves. The inset shows the $|E_0(0)|^2$-dependence of the efficiency $\eta_{\text{AS, peak},\varepsilon} = |E_1|^2_{\text{peak},\varepsilon}/|E_0(0)|^2$ when β_{TPA} is varied from 0 to 1 (cm/GW).

TPA-induced carriers is indispensable for device applications.

Here, without including FCA with the help of the p-n junction, we can discuss TPA on the peak value $|E_1|^2_{\text{peak},\varepsilon}$ at $z = z_{\text{peak}}$ for $\varepsilon = 0, 0.5, 1$. This is shown in Fig. 11 when using $\beta_{\text{TPA}} = 0.1$ (cm/GW) measured for TE-modes [48], where the black curves depict $|E_1|^2_{\text{peak},\varepsilon}$ with $\beta_{\text{TPA}} = 0.1$ (cm/GW) and the blue curves show that with $\beta_{\text{TPA}} = 0$ (cm/GW) for a comparison. In Fig. 11, we can see that a decrease in $|E_1|^2_{\text{peak},\varepsilon}$ due to non-zero β_{TPA} becomes larger for smaller ε, where at smaller ε, the anti-Stokes-wave intensity is larger and thus there is stronger TPA.

In the inset of Fig. 11, we plot the peak output efficiency $\eta_{\text{AS, peak},\varepsilon} = |E_1|^2_{\text{peak},\varepsilon}/|E_0(0)|^2$ for some different β_{TPA}'s between 0 and 1 (cm/GW) when $|E_0(0)|^2 = 4.0$ (GW/cm^2), because a different value of $\beta_{\mathrm{TPA}} = 0.35$ (cm/GW) from 0.1 (cm/GW) has been reported [33]. In the inset, we observe that $\eta_{\mathrm{AS,\,peak},\,\varepsilon}$ decreases rapidly with increasing β_{TPA}, where the decrease is more rapid for smaller ε because of stronger TPA with larger $|E_1|^2_{\mathrm{peak},\,\varepsilon}$.

In the above, a great decrease in the output efficiency η_{AS} due to TPA has been shown quantitatively, and we recognize the significance of keeping λ_i $(i = -1, 0, 1)$ near and larger than λ_{half} to avoid TPA and obtain highly-efficient output for device applications.

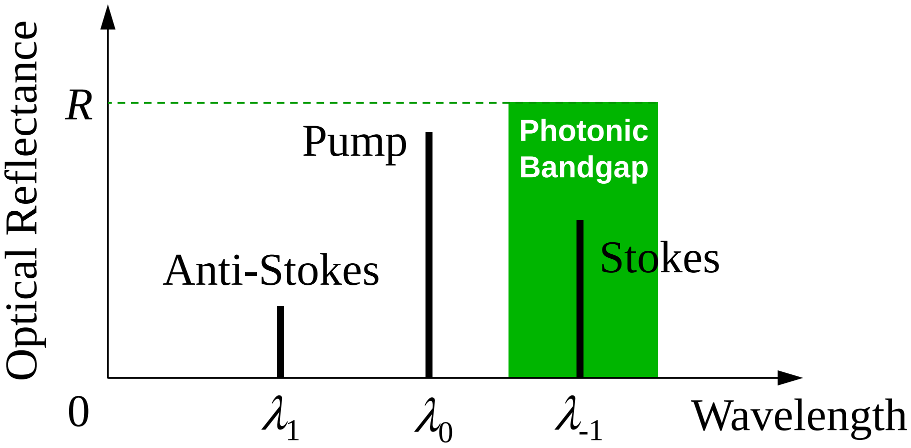

FIG. 12. Optical reflectance for DMMs or PhCs (with $0 < R < 1$ by controlling the DMM or PhC size) that form a cavity, where they reflect the Stokes waves back to the device with their bandgap and let the pump and anti-Stokes waves go through them. By this method, the enhancement in the Stokes-wave intensity $|E_{-1}|^2$ provides high anti-Stokes efficiency η_{AS} because of $\eta_{\mathrm{AS}} \propto |E_{-1}|^2$.

In order to obtain much larger η_{AS}, we propose a cavity structure with dielectric multilayer mirrors (DMMs) or photonic crystals (PhCs) [49–53] attached to both ends of the device, which can also shorten the device. Here, the DMMs and PhCs have a function that they reflect the Stokes waves back to the device with their bandgap with optical reflectance R to enhance the Stokes-wave intensity $|E_{-1}|^2$ in the device, and let the pump and anti-Stokes waves pass through them, as illustrated in Fig. 12. This enhancement in $|E_{-1}|^2$ increases η_{AS} (with no necessity of boosting the pump intensity $|E_0|^2$) owing to the relation $\eta_{\mathrm{AS}} \propto |E_{-1}|^2$ in Eq. (70). If we use bandgap structures with $R < 1$, it is possible to adjust the sizes of η_{AS} and η_{S} (and to equalize them, if necessary). Quantitative analysis of such efficiency adjustments will be provided in a forthcoming paper.

V. SUMMARY

We have proposed a superlattice SRS device design utilizing a GaAs/AlAs intermixed superlattice with $\chi^{(3)}$-nonlinearity that can boost the anti-Stokes-wave efficiency η_{AS} by QPM at 1.49 μm to the same order of the Stokes-wave efficiency η_{S} at 1.63 μm with the input of a 1.56-μm pump beam, which could be used for channel amplification and/or conversion in GE-PONs and WDM systems.

In particular, having focused on the anti-Stokes-wave amplification, we have computed η_{AS} including the effects of FWM, SPM, and XPM with coupled nonlinear equations for the interacting pump, Stokes, and anti-Stokes waves, because those effects are much stronger than those in Si and SiO_2.

The solutions by an analytical method with approximations and by a numerical method have shown a good agreement at the initial stage of growth of the Stokes and anti-Stokes waves for no QPM case. The analytical solutions have shown that FWM enhances SRS, where the influence of SPM and XPM was greatly reduced in the approximations. The numerical calculations without such approximations have given a result that a difference between the analytical and numerical solutions in behavior out of the initial stage stems from pump depletion and the SPM and XPM effects. To obtain η_{AS} precisely, we have numerically computed it for the cases with and without QPM containing FWM, SPM, and XPM effects. A comparison between the two cases has exhibited that there is a three orders of magnitude greater efficiency with QPM than that without QPM for $\varepsilon \leq 0.5$ at a small pump intensity. The physical mechanism of these has been clearly shown in terms of nonlinear-interaction analysis. A TPA-effect on η_{AS} at an optimal length has also been examined, which indicates the significance of TPA-reduction for device applications. In addition, we have proposed the use of a photonic-bandgap cavity to obtain more η_{AS} or control the sizes of η_{AS} and η_{S}.

The proposed device has potential towards ultrahigh-speed data processing/routing applications using channel conversion and amplification via instantaneous optical nonlinear interactions without any influence of carriers, or electron-hole pairs, that distort the waveforms of optical signals.

ACKNOWLEDGMENT

I. T. would like to thank Koshiyama Science & Technology Foundation for the financial support. S. S. would like to thank EPSRC Standard Grant (EP/M009416/1), EPSRC Manufacturing Fellowship (EP/M008975/1), EPSRC Platform Grant (EP/N013247/1), and the University of Southampton Zepler Institute Research Collaboration Stimulus Fund [54]. D. C. H. would like to thank the research collaboration in the University of Glasgow.

---

[1] Y. Fang, N. Seong, and D. D. Dlott, Measurement of the distribution of site enhancements in surface-enhanced Raman scattering, Science **321**, 388 (2008).

[2] S. Nie and S. R. Emory, Probing single molecules and single nanoparticles by surface-enhanced Raman scattering, Science **21**, 1102 (1997).

[3] R. Claps, D. Dimitropoulos, Y. Han, and B. Jalali, Observation of Raman emission in silicon waveguides at 1.54 μm, Opt Express **10**, 1305 (2002).

[4] R. Claps, D. Dimitropoulos, V. Raghunathan, Y. Han, and B. Jalali, Observation of stimulated Raman amplification in silicon waveguides, Opt. Express **11**, 1731 (2003).

[5] H. Rong, A. Liu, R. Jones, O. Cohen, D. Hak, R. Nicolaescu, A. Fang, and M. Paniccia An all-silicon Raman laser, Nature (London) **433**, 292 (2005).

[6] H. Rong, R. Jones, A. Liu, O. Cohen, D. Hak, A. Fang, and M. Paniccia, A continuous-wave Raman silicon laser, Nature (London) **433**, 725 (2005).

[7] H. Rong, S. Xu, Y. H. Kuo, V. Sih, O. Cohen, O. Raday, and M. Paniccia, Low-threshold continuous-wave Raman silicon laser, Nature Photon. **1**, 232 (2007).

[8] M. N. Islam, Raman amplifiers for telecommunications, IEEE J. Sel. Top. Quantum Electron. **8**, 548 (2002).

[9] K. Suto, T. Kimura, T. Saito, A. Watanabe, and J. Nishizawa, GaP-Al$_x$Ga$_{1-x}$P waveguide Raman lasers and amplifiers for optical communication, Proceedings of the IEEE Twenty-

Fourth International Symposium on Compound Semiconductors, San Diego, USA, 8-11 Sep. 1997, p. 573 (1998).

[10] D. Cotter, R. J. Manning, K. J. Blow, A. D. Ellis, A. E. Kelly, D. Nesset, I. D. Phillips, A. J. Poustie, and D. C. Rogers, Nonlinear optics for high-speed digital information processing, Science **19**, 1523 (1999), Active semiconductor-based switches, p. 1525.

[11] K. Suto, T. Kimura, T. Saito, and J. Nishizawa, Raman amplification in GaP-Al$_x$Ga$_{1-x}$P waveguides for light frequency discrimination, IEE Proceeding of Optoelectronics **145**, 105 (1998).

[12] N. S. Makarov and V. G. Bespalov, Combined Stokes-anti-Stokes Raman amplification in fiber, Proceedings of SPIE **4605**, 280 (2001).

[13] J. Reintjes and M. Bashkansky, *Stimulated Raman and Brillouin Scattering* in Handbook of Optics: Fiber Optics and Nonlinear Optics, Volume IV, 2nd ed. (McGraw Hill, 2001), Chap. 18.

[14] N. S. Makarov and V. G. Bespalov, Effective method of anti-Stokes generation by quasi-phase-matched stimulated Raman scattering, J. Opt. Soc. Am. B **22**, 835 (2005).

[15] P. G. Zverev, T.T. Basiev, V. V. Osiko, A. M. Kulkov, V. N. Voitsekhovskii, and V. E. Yakobson, Physical, chemical and optical properties of barium nitrate Raman crystal, Opt. Materials **11**, 315 (1999).

[16] Y. H. Kao, M. N. Islam, J. M. Saylor, R. E. Slusher, and W. S. Hobson, Raman effect in AlGaAs waveguides for subpicosecond pulses, J. Appl. Phys. **78**, 2198 (1995).

[17] R. W. Boyd, *Nonlinear Optics*, 1st ed. (Academic Press, San Diego, 1992).

[18] O. Boyraz, D. Dimitropoulos, and B. Jalali, Observation of simultaneous Stokes and anti-Stokes emission in a silicon Raman laser, IEICE Electron. Express **1**, 435 (2004).

[19] R. Claps, V. Raghunathan, D. Dimitropoulos, and B. Jalali, Anti-Stokes Raman conversion in silicon waveguides, Opt Express **11**, 2862 (2003).

[20] K. Iwatsuki and K. Tsukamoto, Optical coherent technologies in next generation access networks, Proceedings of SPIE Conference Vol. 8282, Broadband Access Communication Technologies VI, San Francisco, California, USA, 21 Jan. No. 828202 (2012).

[21] J. A. Armstrong, N. Bloembergen, J. Ducuing, and P. S. Pershan, Interactions between light waves in a nonlinear dielectric, Phys. Rev. **127**, 1918 (1962).

[22] A. S. Helmy, D. C. Hutchings, T. C. Kleckner, J. H. Marsh, A. C. Bryce, J. M. Arnold, C. R. Stanley, J. S. Aitchison, C. T. A. Brown, K. Moutzouris, and M. Ebrahimzadeh, Quasi phase matching in GaAs-AlAs superlattice waveguides through bandgap tuning by use of quantum-well intermixing, Opt. Lett. **25**, 1370 (2000).

[23] T. C. Kleckner, A. S. Helmy, K. Zeaiter, D. C. Hutchings, and J. S. Aitchison, Dispersion and modulation of the linear optical properties of GaAs-AlAs superlattice waveguides using quantum-well intermixing, IEEE J. Quantum Electron. **42**, 280 (2006).

[24] S. J. B. Yoo, C. Caneau, R. Bhat, M. A. Koza, A. Rajhel, and N. Antoniades, Wavelength conversion by difference frequency generation in AlGaAs waveguides with periodic domain inversion achieved by wafer bonding, Appl. Phys. Lett. 68, 2609 (1996).

[25] D. C. Hutchings, Modulation of the second-order susceptibility in GaAs/AlAs superlattices, Appl. Phys. Lett. **76**, 1362 (2000).

[26] M. J. A. Smith, B. T. Kuhlmey, C. M. de Sterke, C. Wolff, M. Lapine, and C. G. Poulton, Metamaterial control of stimulated Brillouin scattering, Opt. Lett. **41**, 2338 (2016).

[27] G. P. Agrawal, *Nonlinear Fiber Optics*, 5th ed. (Academic Press, New York, 2013).

[28] D. C. Hutchings, Theory of ultrafast nonlinear refraction in semiconductor superlattices, IEEE J. Sel. Top. Quantum Electron. **10**, 1124 (2004), Sec. IV B.

[29] A. Yariv, *Optical Electronics in Modern Communications*, 5th ed. (Oxford University Press, Oxford, 1997). The slowly-varying-envelop approximation with the spatial width W of propagating pulses larger than their wavelength (1.49-1.63 μm) can be kept for the short pulses with a time width of $\tau \approx 10$ ps because of $W = c\tau/\bar{n} = 3 \times 10^8\,\mathrm{m/s} \times 10\,\mathrm{ps}/3.1 \approx 1000\,\mu\mathrm{m} \gg$ 1.49-1.63 μm, where $c = 3 \times 10^8$ m/s is the light velocity in vacuum and $\bar{n} = 3.1$ is the average refractive index of the device.

[30] Y. R. Shen and N. Bloembergen, Theory of Stimulated Brillouin and Raman Scattering, Phys. Rev. **137**, A1787 (1965).

[31] P. Weidner and A. Penzkofer, Spectral broadening of picosecond laser pulses in optical fibres, Optical and Quantum Electronics **25**, 1 (1993).

[32] S. J. Wagner, J. Meier, A. S. Helmy, J. S. Aitchison, M. Sorel, and D. C. Hutchings, Polarization-dependent nonlinear refraction and two-photon absorption in GaAs/AlAs superlattice waveguides below the half-bandgap, J. Opt. Soc. Am. B **24**, 1557 (2007).

[33] A. Villeneuve, C. C. Yang, G. I. Stegeman, C. H. Lin, and H. H. Lin, Nonlinear refractive-index and two photon-absorption near half the band gap in AlGaAs, Appl. Phys. Lett. **62**, 2465 (1993).

[34] M. Dinu, F. Quochi, and H. Garcia, Third-order nonlinearities in silicon at telecom wavelengths, Appl. Phys. Lett. **82**, 2954 (2003).

[35] L. Xu, P. K. A. Wai, and H. Y. Tam, Raman-assisted four-wave mixing, Proceedings of the Sixth Chinese Optoelectronics Symposium, Hong Kong University of Science and Technology, Hong Kong, China, 12 - 14 Sep. 2003, p. 169 (2003).

[36] W. H. Press, S. A. Teukolsky, W. T. Vetterling, and B. P. Flannery, *Numerical Recipes in Fortran 90 - The Art of Parallel Scientific Computing: Vol.2*, 2nd ed. (Cambridge University Press, Cambridge, 1996).

[37] D. C. Hutchings and B. S. Wherrett, Theory of the dispersion of ultrafast nonlinear refraction in zinc-blende semiconductors below the band edge, Phys. Rev. B **50**, 4622 (1994).

[38] D. C. Hutchings and B. S. Wherrett, Theory of the anisotropy of ultrafast nonlinear refraction in zinc-blende semiconductors, Phys. Rev. B **52**, 8150 (1995).

[39] Y. P. Varshni, Temperature dependence of the energy gap in semiconductors, Physica **34**, 149 (1967).

[40] C. Bosio, J. L. Staehli, M. Guzzi, G. Burri, and R. A. Logan, Direct-energy-gap dependence on Al concentration in $\mathrm{Al}_x\mathrm{Ga}_{1-x}\mathrm{As}$, Phys. Rev. B **38**, 3263 (1988).

[41] S. Logothetidis, M. Cardona, and M. Garriga, Temperature dependence of the dielectric function and the interband critical-point parameters of $\mathrm{Al}_x\mathrm{Ga}_{1-x}\mathrm{As}$, Phys. Rev. B **43**, 11950 (1991).

[42] J. T. Boyd, Theory of parametric oscillation phase matched in GaAs thin-film waveguides, IEEE J. Quantum Electron. **8**, 788 (1972).

[43] M. Ilegems and G. L. Pearson, Infrared reflection spectra of $\mathrm{Ga}_{1-x}\mathrm{Al}_x\mathrm{As}$ mixed crystals, Phys. Rev. B **1**, 1576 (1970).

[44] G. A. Porkolab, P. Apiratikul, B. Wang, S. H. Guo, and C. J. K. Richardson, Low propagation loss AlGaAs waveguides fabricated with plasma-assisted photoresist reflow, Opt. Express **22**, 7733 (2014).

[45] Use of a very small waveguide cross-sectional area, e.g., $(0.1\ \mu\mathrm{m})^2$, which is now technically feasible, can greatly reduce the pump power, e.g., to 400 mW. This gives a large structural

dispersion to Eq. (73). If this is included to determine the QPM period Λ, the pump power (400 mW) is possible.

[46] SRS threshold intensity δ, e.g., at a maximum observed in Si waveguides [5–7], is used here, because the Raman gain g is on the same order of magnitude between Si and $\mathrm{Al}_x\mathrm{Ga}_{1-x}\mathrm{As}$ (or GaAs/AlAs superlattices).

[47] N. Suzuki, FDTD analysis of two-photon absorption and free-carrier absorption in Si high-index-contrast waveguides, J. Lightwave Tech. **25**, 2495 (2007).

[48] J. S. Aitchison, D. C. Hutchings, J. U. Kang, G. I. Stegeman, and A. Villeneuve, The nonlinear optical properties of AlGaAs at the half band gap, IEEE J. Quantum Electron. **33**, 341 (1997).

[49] I. Tomita, Highly efficient cascaded difference-frequency generation in periodically poled LiNbO_3 devices with resonators, IEEJ Trans. Electrical & Electronic Eng. (2018), accepted.

[50] E. Yablonovitch, Inhibited spontaneous emission in solid-state physics and electronics, Phys. Rev. Lett. **58**, 2059 (1987).

[51] S. John, Strong localization of photons in certain disordered dielectric superlattices, Phys. Rev. Lett. **58**, 2486 (1987).

[52] E. Yablonovitch, Photonic crystals: Semiconductors of light, Sci. Am. **285**, 46 (2001).

[53] J. D. Joannopoulos, S. G. Johnson, J. N. Winn, and R. D. Meade, *Photonic Crystals - Molding the Flow of Light*, 2nd ed. (Princeton University Press, New Jersey, 2008).

[54] The data in the paper can be obtained from the University of Southampton ePrint research repository: http://dx.doi.org/10.5258/SOTON/D0238.